Article

Neuroprosthetic baroreflex controls haemodynamics after spinal cord injury

https://doi.org/10.1038/s41586-020-03180-w

Received: 7 May 2020

Accepted: 11 December 2020

Published online: 27 January 2021

Check for updates

Jordan W. Squair[1,2,3,4,5,6,7,8,9,10], Matthieu Gautier[1,4,24], Lois Mahe[1,4,24], Jan Elaine Soriano[5,6,7,10,24], Andreas Rowald[1,4,24], Arnaud Bichat[1,4], Newton Cho[1,4,11], Mark A. Anderson[1,4], Nicholas D. James[1,4], Jerome Gandar[1,4], Anthony V. Incognito[10,12], Giuseppe Schiavone[13], Zoe K. Sarafis[1,4], Achilleas Laskaratos[1,4], Kay Bartholdi[1,4], Robin Demesmaeker[1,4], Salif Komi[1,4], Charlotte Moerman[3,4], Bita Vaseghi[5,6,7], Berkeley Scott[5,6,7,10], Ryan Rosentreter[5,6,7,10], Claudia Kathe[1,4], Jimmy Ravier[1,4], Laura McCracken[1,4], Xiaoyang Kang[13], Nicolas Vachicouras[13], Florian Fallegger[13], Ileana Jelescu[14], YunLong Cheng[15], Qin Li[15], Rik Buschman[16], Nicolas Buse[16], Tim Denison[17,18], Sean Dukelow[5,6,7,10,19], Rebecca Charbonneau[6,10], Ian Rigby[20], Steven K. Boyd[19], Philip J. Millar[12], Eduardo Martin Moraud[3,4], Marco Capogrosso[21], Fabien B. Wagner[1,4,22], Quentin Barraud[1,4], Erwan Bezard[15,22,23], Stéphanie P. Lacour[13], Jocelyne Bloch[1,2,3,4], Grégoire Courtine[1,2,3,4,25] ✉ & Aaron A. Phillips[5,6,7,9,10,25] ✉

Spinal cord injury (SCI) induces haemodynamic instability that threatens survival[1–3], impairs neurological recovery[4,5], increases the risk of cardiovascular disease[6,7], and reduces quality of life[8,9]. Haemodynamic instability in this context is due to the interruption of supraspinal efferent commands to sympathetic circuits located in the spinal cord[10], which prevents the natural baroreflex from controlling these circuits to adjust peripheral vascular resistance. Epidural electrical stimulation (EES) of the spinal cord has been shown to compensate for interrupted supraspinal commands to motor circuits below the injury[11], and restored walking after paralysis[12]. Here, we leveraged these concepts to develop EES protocols that restored haemodynamic stability after SCI. We established a preclinical model that enabled us to dissect the topology and dynamics of the sympathetic circuits, and to understand how EES can engage these circuits. We incorporated these spatial and temporal features into stimulation protocols to conceive a clinical-grade biomimetic haemodynamic regulator that operates in a closed loop. This 'neuroprosthetic baroreflex' controlled haemodynamics for extended periods of time in rodents, non-human primates and humans, after both acute and chronic SCI. We will now conduct clinical trials to turn the neuroprosthetic baroreflex into a commonly available therapy for people with SCI.

An SCI immediately impairs haemodynamic stability, and leads to repeated hypotensive episodes that are life threatening and reduce neurological recovery[1,4,5,13,14]. Daily hypotensive episodes augment the risk of stroke and heart disease[6,7,15], and reduce engagement in social and professional activities[8,9].

This haemodynamic instability is due to the interruption of supraspinal drive to the sympathetic circuitry. Consequently, this circuitry no longer receives efferent commands from brainstem vasomotor regulatory centres, and prevents the natural baroreflex from exerting precise control over the sympathetic circuitry that adjusts peripheral vascular resistance[16,17]. EES can compensate for missing regulatory commands from the brain after a SCI[12,18–20]. For example, the delivery of EES with a spatial and temporal sequence that coincides with the ongoing movement reinstated the natural dynamics of motor neuron activation, which restored locomotion after SCI[11,12,21]. Serendipitous observations showed that EES applied over lumbosacral segments can also transiently increase blood pressure[22–25]. However, lumbosacral segments contain few sympathetic efferent neurons, casting doubt that this approach harnesses the full potential of EES to activate sympathetic circuits and achieve haemodynamic stability after SCI.

Here, we uncovered the key mechanisms through which EES modulates blood pressure, and leveraged this understanding to conceive a neuroprosthetic baroreflex that precisely controlled haemodynamics over extended periods of time in rodents, non-human primates and humans, and was effective from a few hours after SCI to the chronic phase of the condition.

Preclinical model of haemodynamic instability

Rats received a severe clinically relevant contusion onto thoracic (T3) segments (Fig. 1a, Extended Data Fig. 1). To visualize how this contusion damaged the descending pathways that regulate haemodynamics, we targeted catecholaminergic neurons expressing tyrosine hydroxylase (TH) by stereotaxic infusions of the adeno-associated virus

A list of affiliations appears at the end of the paper.

AAV-DJ-hSyn-flex-mGFP-2A-synaptophysin-mRuby[26] into the rostral ventrolateral medulla (RVLM) of TH-Cre rats[27]. CLARITY-optimized light-sheet microscopy[28] of TH-positive (TH^{ON}) fibres and synapses revealed a near complete depletion of sympatho-excitatory synapses onto choline acetyltransferase-positive ($ChAT^{ON}$) sympathetic preganglionic neurons below the injury (Fig. 1a).

To characterize the natural history of haemodynamic instability after SCI, we implanted rats with a wireless system that enabled 24/7 monitoring of arterial blood pressure and sympathetic nerve activity (Fig. 1b, Extended Data Fig. 1d–g). The SCI instantly induced a transient spike in blood pressure and sympathetic nerve activity (Extended Data Fig. 2a–c), followed by a pronounced depression that persisted throughout the chronic phase (Fig. 1d). The 24/7 monitoring of blood pressure and sympathetic nerve activity in the home cage showed that the SCI led to profound haemodynamic instability (Extended Data Fig. 2d–g).

Despite the elimination of the sympathetic-vasomotor division of the natural baroreflex, the rats did not exhibit the hypotension observed in humans in response to orthostatic challenges (Extended Data Fig. 1a), thus preventing the investigation of this specific physiological mechanism in preclinical models.

To enable such investigations, we developed a servo-controlled negative-pressure chamber that mimics orthostatic challenge paradigms used in humans to quantify haemodynamic instability (Fig. 1c). Uninjured rats exposed to negative pressure exhibited transient hypotensive episodes. After SCI, rats could no longer recover from the simulated orthostatic challenge (Fig. 1d). They exhibited sustained hypotension, the severity of which linearly correlated with the pressure in the chamber (Extended Data Fig. 2h–j).

These results indicate that our preclinical model reproduced the hallmarks of haemodynamic instability observed in humans, and thus established heuristic conditions to dissect the mechanisms through which EES could regulate haemodynamics after SCI.

EES engages sympathetic circuitry

Clinical observations reported pressor responses when applying EES over lumbosacral segments[22–25], but the mechanisms that underlie these responses remain unknown. We reasoned that understanding these mechanisms would be necessary to develop a therapy that manages haemodynamic instability with maximal efficacy.

We first investigated whether the location of EES was important to trigger pressor responses. We quantified the increase in blood pressure resulting from continuous EES (50 Hz, motor threshold)[21] applied sequentially to each spinal segment, from T6 to L1. The pressor response to EES followed a Gaussian distribution that peaked around the low thoracic segments (Fig. 2a, Extended Data Fig. 3c, d). These responses were observed within a few hours after SCI and throughout the chronic phase of injury (Extended Data Fig. 3d).

Next, we asked whether this distribution of the pressor response matched the topological organization of the sympathetic circuitry[29]. To expose the anatomical distribution of sympathetic pre-ganglionic neurons in the spinal cord, we injected a retrograde tracer in the splanchnic sympathetic ganglia, which can control blood pressure (Extended Data Fig. 3a). We found retrogradely labelled neurons throughout the well-established spinal cord topology, but a peak concentration of neurons was identified in the caudal thoracic segments (Fig. 2a, Extended Data Fig. 3b). Pressor responses to EES linearly correlated with the density of these neurons, revealing a clear anatomical and functional enrichment at T11–T13 (Fig. 2a, Extended Data Fig. 3e). We named these segments the haemodynamic hotspots.

We then investigated the neural substrates recruited by EES that trigger pressor responses. We first modelled the electrical fields elicited by EES using a previously validated finite element method[30] that we complemented with magnetic resonance imaging (MRI), computerized-tomography, and anatomical reconstructions of the thoracic spine (Fig. 2c). Simulations predicted that EES primarily recruits large-diameter afferent fibres located in the posterior roots, but has no direct influence on intraspinal neurons or on efferent pathways from sympathetic pre-ganglionic neurons (Extended Data Fig. 4a).

To test this prediction, we asked whether the thoracic posterior roots that project to the haemodynamic hotspots were necessary to elicit pressor responses with EES. We found that the progressive ablation of these roots led to the graded suppression of pressor responses (Fig. 2c, Extended Data Fig. 4b).

Previous clinical studies reported pressor responses when stimulating rostral lumbar segments[22–25], which contrasts with our finding that pressor responses elicited by EES require the recruitment of the posterior roots projecting to the caudal thoracic segments (Fig. 2a). We thus studied the mechanisms that could explain these observations. Computer simulations suggested that EES applied at L2 can recruit the caudal thoracic posterior roots where they bend and pass through the inter-vertebral foramen. Indeed, ablation of the T12 posterior roots blunted the modest pressor responses elicited by EES applied at L2 (Extended Data Fig. 3f). These results suggest that the incidental recruitment of T12 posterior roots at the level of L2 may mediate the pressor responses observed in previous clinical studies[22–25].

We next sought to confirm that EES engages sympathetic circuitry to elicit pressor responses. We tested whether EES recruits splanchnic sympathetic ganglion neurons, and whether their efferent pathways trigger pressor responses. Delivering EES for 30 min induced a robust expression of the activity-dependent protein FOS in TH^{ON} neurons located in splanchnic sympathetic ganglia (Fig. 2d). To ascertain their causal role, we expressed the light-sensitive eNpHR3.0 opsin[31] in these neurons using targeted injections of AAV5-hSyn-eNpHR3.0-YFP in splanchnic sympathetic ganglia. Silencing of these neurons with light or ablating their efferent pathways blunted the pressor response to EES (Fig. 2e, Extended Data Fig. 5c, d). These efferent neurons release noradrenaline that induces constriction of blood vessels through the activation of α_1 receptors. We blocked these receptors with intravenous injections of prazosin[32], which reversibly suppressed responses to EES (Fig. 2f, Extended Data Fig. 5e).

These results show that the depolarization of afferent fibres in the posterior roots leads to the activation of splanchnic sympathetic ganglion neurons, which indicated that connections exist between afferent fibres and sympathetic pre-ganglionic neurons. We therefore labelled afferent projections with co-injections of AAV-DJ-hSyn-flex-mGFP-2A-synaptophysin-mRuby and AAV-Cre into T12 dorsal root ganglia. We developed a pipeline to dynamically warp spinal cord contours to a histological atlas, allowing us to merge data from several tissue sections and rats (Extended Data Fig. 4d). Spatial analysis of merged matrices revealed an absence of afferent axons and synapses within the intermediolateral column that contains the vast majority of sympathetic pre-ganglionic neurons[29] (Extended Data Fig. 4d). We confirmed the absence of the traced synaptic projections onto sympathetic pre-ganglionic neurons by immunolabelling them with ChAT. Therefore, the connection between afferent fibres and sympathetic pre-ganglionic neurons probably involves an excitatory interneuron (Extended Data Fig. 4c). Time-dependent pseudorabies-mediated tracing revealed the presence of glutamatergic interneurons connected trans-synaptically to splanchnic sympathetic ganglionic neurons (Fig. 2g, Extended Data Fig. 4d). These interneurons were densely innervated by $VGLUT1^{ON}$ synapses from proprioceptive neurons[33] (Fig. 2h), supporting the existence of indirect connections between afferent fibres and sympathetic preganglionic neurons through an excitatory interneuron.

Together, these results identify key mechanisms that underlie pressor responses elicited by EES. First, to maximize pressor responses, EES must target the spinal segments containing the highest density of sympathetic pre-ganglionic neurons that project to splanchnic neurons. Second, EES relies on the afferent fibres in the posterior roots to

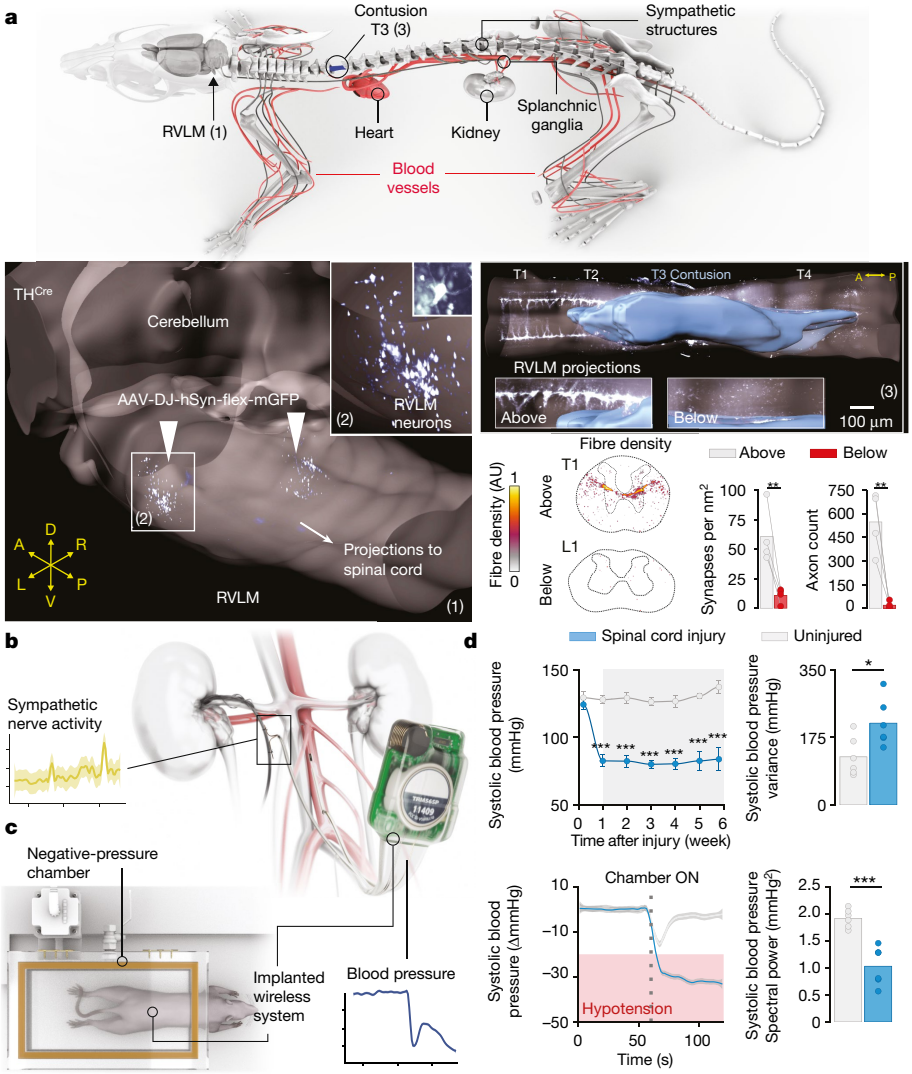

Fig. 1 | Preclinical model overview. a, Rodent experimental model. RVLM TH^{ON} neurons and their projections after SCI. Bar charts show the mean fibre density above and below SCI ($n = 4$) (paired one-tailed t-test; $t = 5.08$; $P = 0.007$) and synapses (paired one-tailed t-test; $t = 4.64$; $P = 0.009$). T1 to T4 denote first to fourth thoracic spinal segments. **b**, Wireless telemetry system to record haemodynamics and sympathetic nerve activity 24/7. **c**, Negative-pressure chamber to simulate an orthostatic challenge. **d**, Resting blood pressure before and up to 6 weeks after injury ($n = 6$, two-way repeated-measures analysis of variance (ANOVA), Tukey's honestly significant difference (HSD); $F_{(1,6)\text{interaction}} = 7.05$; $P = 1.10 \times 10^{-5}$; all post hoc $P < 0.001$). Data are mean ± s.e.m. Bar charts show haemodynamic variance ($n = 6$, independent samples one-tailed t-test; $t = 2.70$; $P = 0.011$) (top) and low frequency pressure dynamics ($n = 6$, independent samples one-tailed t-test; $t = 5.51$; $P = 0.0004$) (bottom). The line plot illustrates orthostatic intolerance after injury and when exposed to lower body negative pressure. *$P < 0.05$; **$P < 0.01$; ***$P < 0.001$.

engage the sympathetic circuitry. Third, EES leads to the activation of splanchnic sympathetic ganglion neurons, which constrict blood vessels and increase blood pressure. These three key results provide a mechanistic framework to develop neurotechnologies to manage haemodynamic instability with EES.

Biomimetic closed-loop haemodynamic control

We exploited this knowledge to configure electronic dura mater (e-dura) implants[34] that targeted the posterior roots projecting to the six haemodynamic hotspots. Optimal electrode numbers and locations were identified using a genetic algorithm[12,21] implemented in the computational model. We optimized the geometry of e-dura implants to conform to the curved topology of the thoracic spinal column (Extended Data Fig. 6a–c).

Neuromodulation strategies that mimic natural dynamics are more effective than unspecific protocols[12,21,35]. Moreover, non-physiological manipulation of haemodynamics may damage the central nervous system and circulatory system while predisposing to adverse events[36–38]. We therefore aimed to deliver EES patterns that mimic the natural dynamics of sympathetic circuitry activation. To capture these dynamics, we recorded sympathetic nerve activity and haemodynamics (Extended Data Fig. 6d). Feed-forward, artificial neural networks confirmed the disrupted link between haemodynamics and sympathetic circuitry after SCI (Extended Data Fig. 6d). Wavelet decomposition analysis[39] of blood pressure signals showed that blue-light photostimulation of channelrhodopsin-2-positive (ChR2^{ON}) TH^{ON} neurons located in the RVLM steers haemodynamics within specific frequency domains[40] confined around 0.4–1.0 Hz (Fig. 3a). Orthostatic challenges enhanced haemodynamic activity within the same frequency band in uninjured rats (Fig. 3b). This drive was permanently interrupted after SCI (Fig. 3b).

We then measured the rostrocaudal transmission of descending sympathetic volleys (Extended Data Fig. 6e), which we quantified from the propagation of surface potentials over the haemodynamic hotspots

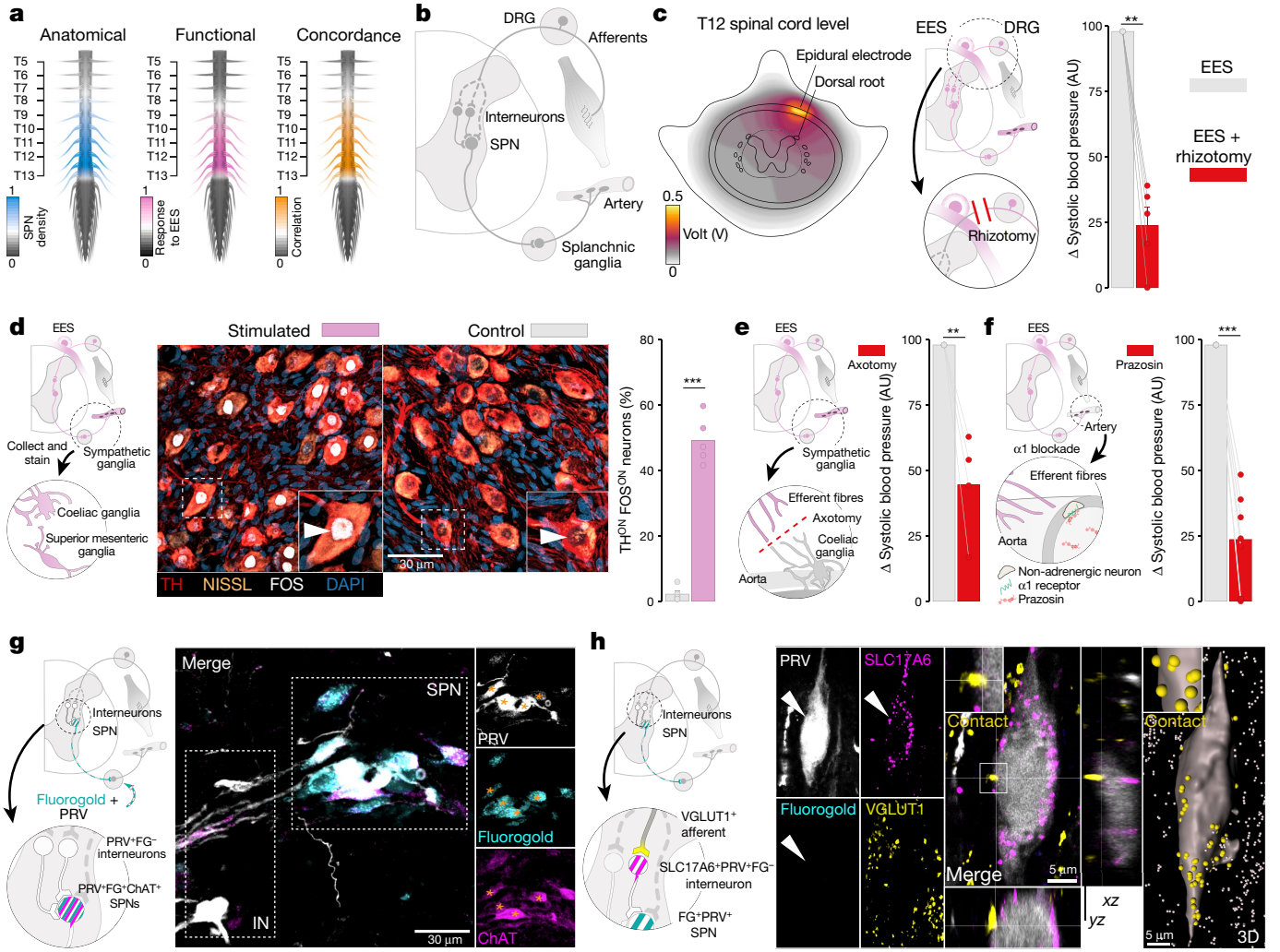

Fig. 2 | Mechanisms by which EES stabilizes haemodynamics. a, Intraspinal density of neurons retrogradely traced from the splanchnic ganglia one month after injury, amplitude of pressor responses to EES, and concordance between anatomical and functional datasets. Mean data are shown for $n = 5$ rats. **b**, Hypothetical circuits activated by EES to elicit blood vessel constriction. DRG, dorsal root ganglia. **c**, Electrical potentials elicited by EES. Bar charts show pressor responses to EES before and after rhizotomy ($n = 5$, paired samples one-tailed t-test; 18.3 mmHg versus 5.7 mmHg; $t = 4.36$; $P = 0.006$). AU, arbitrary units. **d**, FOS expression in TH^{ON} neurons in the splanchnic ganglia. Bar chart shows percentage of FOS^{ON} neurons ($n = 5$, independent samples one-tailed t-test; $t = 13.96$; $P = 2.49 \times 10^{-5}$). **e**, Ablation of splanchnic efferent neurons blunted the pressor response ($n = 4$, paired samples one-tailed t-test; 20.0 mmHg versus 9.2 mmHg; $t = -4.54$; $P = 0.0099$). **f**, Blockade of α_1 receptor with prazosin resulted in blunted pressor responses ($n = 5$, paired samples one-tailed t-test; 18.0 mmHg versus 5.7 mmHg; $t = -5.59$; $P = 0.0007$). **g**, Trans-synaptic retrograde tracing revealing interneurons connected to splanchnic ganglia. FG, Fluorogold; PRV, pseudorabies; IN, interneuron; SPN, sympathetic pre-ganglionic neuron. **h**, These interneurons express the excitatory marker *Slc17a6*, and receive VGLUT1 synapses from proprioceptive afferents.

in response to stimulation of RVLM neurons. We found a conduction delay of 2.5 ms between activation of adjacent hotspots.

We encoded these biometrics into EES protocols that mimic the spatial sequences, frequency contents and temporal profiles underlying natural sympathetic circuit activation. This biomimetic stimulation reinstated the natural dynamics of the system (Fig. 3c, Extended Data Fig. 6f), and triggered greater pressor responses than conventional EES protocols (Extended Data Fig. 7a, b).

The management of haemodynamic instability logically necessitates constant titration of EES. We found that biomimetic stimulation led to pressor responses that linearly correlated with EES amplitude ($R^2 = 0.81$; $P = 1.02 \times 10^{-15}$). Therefore, we implemented a proportional-integral controller that modulated biomimetic EES protocols to target user-defined blood pressure levels in a closed loop[21] (Fig. 3d). This haemodynamic regulator updates EES amplitudes in real-time to prevent hypotension (Fig. 3e, f). We thus conceived a neuroprosthetic baroreflex that rapidly (1.15 s, 95% confidence interval: 0.36–2.50) stabilized haemodynamics during transient, varying and sustained orthostatic challenges, after both acute and chronic SCI (Fig. 3e–h, Extended Data Fig. 7c–g).

Translating the neuroprosthetic baroreflex

We next asked whether this neuroprosthetic baroreflex could stabilize haemodynamics immediately after SCI using clinical-grade neurotechnologies[11,12] (Extended Data Fig. 8c). We emulated neuro-intensive care in a non-human primate model that included general propofol-based anaesthesia, an arterial pressure line, and artificial ventilation (Fig. 4a, Extended Data Fig. 8a, b).

We mapped pressor responses to EES across the thoracic and lumbar spinal cords of three rhesus monkeys with acute complete upper-thoracic (T3) SCI, which confirmed the location of haemodynamic hotspots within the three most caudal thoracic segments (Extended Data Fig. 9a, b).

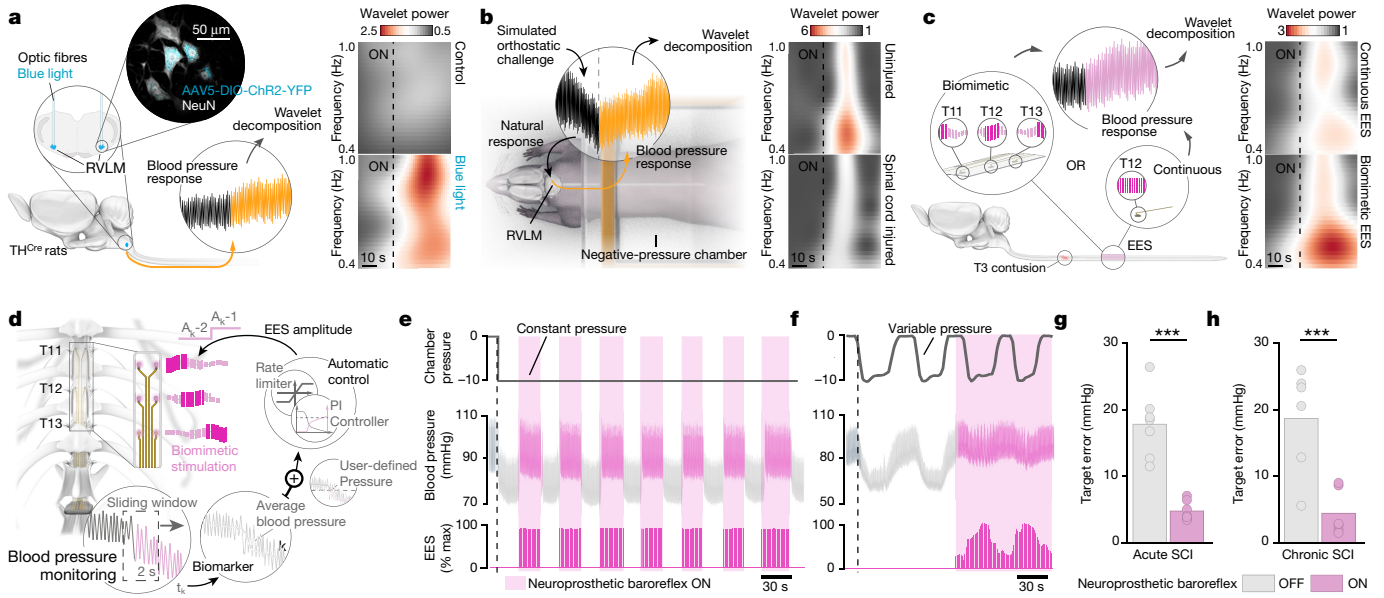

Fig. 3 | The neuroprosthetic baroreflex control haemodynamics. **a**, Targeted expression of ChR2 in TH^{ON} neurons of the RVLM. Wavelet power spectrum when illuminating the RVLM with yellow (control) versus blue light (paired samples one-tailed *t*-test; $t = 2.67$; $P = 0.028$). NeuN, neuronal nuclei. **b**, Wavelet spectrogram when inducing a simulated orthostatic challenge ($n = 6$; independent samples one-tailed *t*-test; $t = 3.01$; $P = 0.0013$). **c**, Biomimetic stimulation protocols, composed of interleaved (2.5 ms) EES (50 Hz) propagating over the haemodynamic hotspots. Wavelet spectrogram in rats with SCI ($n = 5$, paired samples one-tailed *t*-test; $t = 2.31$; $P = 0.041$). **d**, Closed-loop stabilization of blood pressure using a proportional integral (PI) controller that adjusts the amplitude of traveling EES waves over the three haemodynamic hotspots to maintain a defined blood pressure (target). **e**, Pressure in the chamber (top), blood pressure (middle) and EES amplitude (bottom) while the neuroprosthetic baroreflex is turned on and off sequentially. Representative example from one rat shown ($n = 7$ total). **f**, Variables as in **e** shown for cyclical changes in the pressure of the chamber. Representative example from one rat shown ($n = 7$ total). **g**, **h**, Bar charts show errors in blood pressure with respect to the user-defined target with the neuroprosthetic baroreflex on and off, tested in rats with acute SCI (12 h after injury, $n = 7$, paired samples one-tailed *t*-test; systolic blood pressure (SBP): $t = -5.85$, $P = 5.50 \times 10^{-4}$) (**g**) and chronic SCI (6 weeks, $n = 6$, paired samples one-tailed *t*-test; SBP: $t = -3.84$, $P = 0.006$) (**h**).

To modulate these haemodynamic hotspots, we designed e-dura implants[34] with electrode configurations that targeted the left and right posterior roots of T10, T11 and T12 segments. We scaled the implants developed for rats to the anatomical features of rhesus monkeys, measured in three animals (Extended Data Fig. 9c). We connected these e-dura implants to a clinical-grade implantable pulse generator with wireless communication modules and custom-made software interfaces that enable real-time control over spatial locations, temporal sequences and amplitudes of EES[12]. We injected all the features of the neuroprosthetic baroreflex within this versatile stimulation platform (Extended Data Fig. 8c).

The SCI induced an immediate spike in blood pressure, rapidly followed by pronounced hypotension that is reminiscent of life-threatening haemodynamic instability observed acutely in humans with SCI (Extended Data Fig. 8d, e).

As early as a few hours after the SCI, the neuroprosthetic baroreflex instantly normalized blood pressure, stabilizing haemodynamics for extensive periods of time without the need for supervision (2,000 heartbeats shown in Fig. 4b). In contrast to closed-loop EES, pressor responses induced by continuous EES were extinguished after a few heartbeats in this acute phase of SCI (Extended Data Fig. 9g, h). The neuroprosthetic baroreflex maintained haemodynamic stability despite pronounced orthostatic challenges induced in a negative-pressure chamber adapted to monkeys (Fig. 4c, Extended Data Fig. 9f, i). During haemodynamic collapse, the neuroprosthetic baroreflex rescued haemodynamic stability (Fig. 4d, Supplementary Video 1).

Clinical implementation

We finally aimed to validate the key features of the neuroprosthetic baroreflex in a patient presenting with a chronic clinically complete (American Spinal Injury Association Impairment Scale A) cervical SCI that led to debilitating, medically refractory orthostatic hypotension (Extended Data Fig. 10a).

A paddle electrode array was surgically positioned below the T10 and T11 vertebral bodies that contain the posterior roots entering lower thoracic segments (Extended Data Fig. 10a). Computer simulations predicted the optimal electrode configurations[12] to target the haemodynamic hotspots identified in preclinical models (Fig. 4e). EES induced robust pressor responses (Fig. 4f), whereas stimulation delivered more caudally or over electrodes non-specific for the posterior roots (midline) was comparatively far less effective (Extended Data Fig. 10c, d). These results reinforced our conclusions that EES recruits the afferent fibres in the posterior roots to engage the sympathetic circuitry. EES increased sympathetic nerve activity and normalized circulating levels of noradrenaline, which confirmed the activation of the sympathetic circuitry (Fig. 4g).

Next, we sought to determine whether EES could regulate haemodynamics in a closed loop. As observed in preclinical models, we found a linear relationship between EES amplitudes and pressor responses (Extended Data Fig. 10e). Closed-loop adjustment of EES amplitude led to real-time haemodynamic stabilization during orthostatic challenges on a tilt-table (Fig. 4h, Extended Data Fig. 10f, g).

Long-term implementation of EES enabled the permanent cessation of medical treatments for haemodynamic stabilization, increased participation in verticalized motor rehabilitation, and abolished the clinical burden of orthostatic hypotension (Extended Data Fig. 10h, Supplementary Video 2).

Discussion

We developed and validated an ultrafast, highly reliable neuroprosthetic baroreflex that precisely stabilizes haemodynamics in the acute

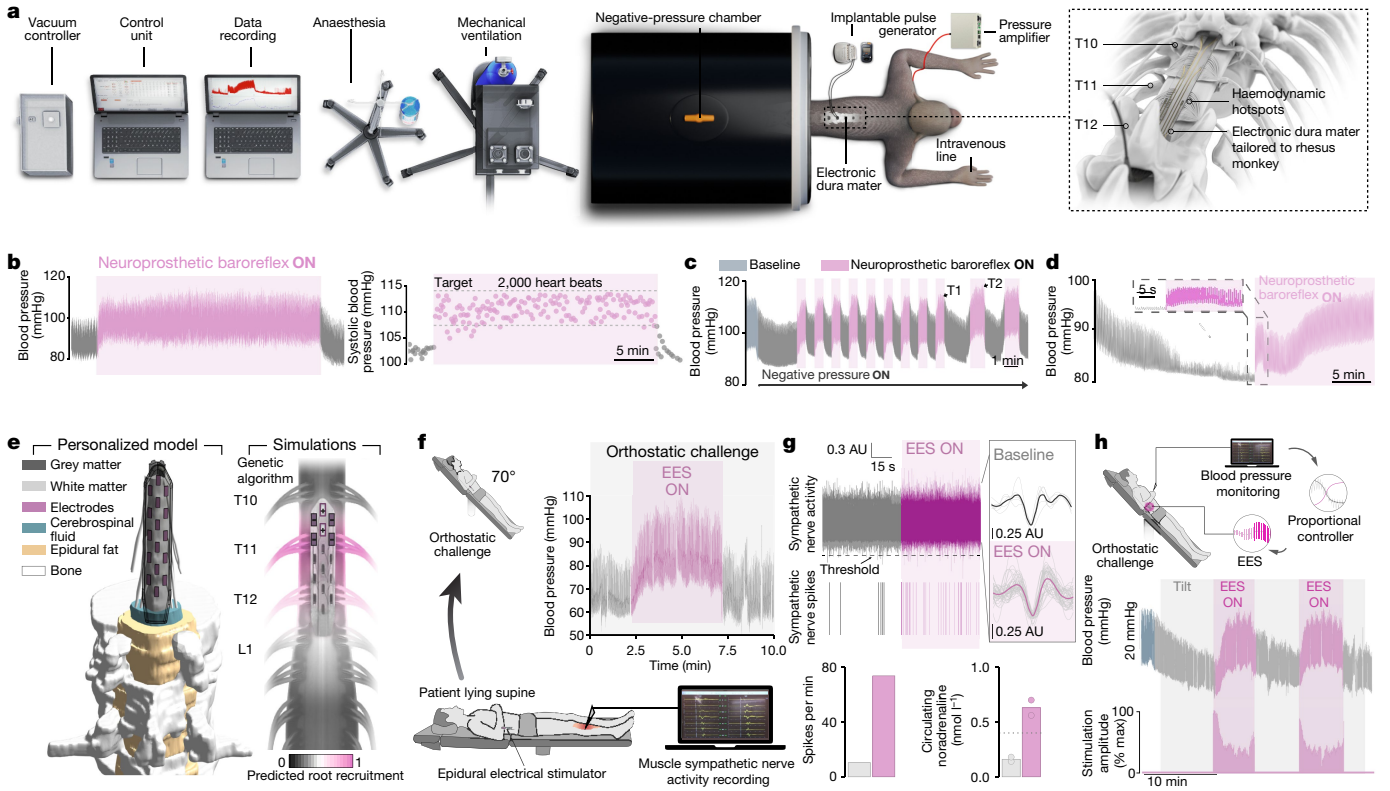

Fig. 4 | Translation of the neuroprosthetic baroreflex. a, Neurointensive care unit for monkeys with acute complete upper thoracic SCI, placed in a negative-pressure chamber. The neuroprosthetic baroreflex is implemented using clinical-grade technologies operated with a custom-made software. **b**, Blood pressure with the neuroprosthetic baroreflex on for 2,000 heartbeats. **c**, Experiments as in Fig. 3e. **d**, Blood pressure collapse, rescued by the neuroprosthetic baroreflex. **e**, Computational model of the human participant, including predicted spatial configurations to target the cardiovascular hotspots. **f**, Orthostatic challenge on a tilt table. Pressor response with EES. **g**, Muscle sympathetic nerve activity (MSNA) recording from the peroneal nerve without and with EES. Bar charts show MSNA spike rates and levels of circulating noradrenaline. Horizontal dotted line represents the minimum reference range. **h**, Pressor responses during closed-loop EES concomitant to orthostatic challenges.

and chronic phases of SCI. Central to this development was an experimental preclinical model of haemodynamic instability that enabled the identification of the topology and dynamics of natural sympathetic circuit activation. We combined this fundamental knowledge with a new understanding of the key mechanisms through which EES activates the sympathetic circuitry to conceive biomimetic protocols that obey guidelines for ecoprosthetic designs[41]. The evolutionary conservation of the ancestral sympathetic circuitry enabled straightforward translation of these protocols from rats to non-human primates and humans.

We implemented this neuroprosthetic baroreflex within an implantable stimulation platform that we previously used to restore walking in humans with paralysis[12]. We validated this neuroprosthetic baroreflex in non-human primates. Experiments in one patient with tetraplegia indicated that the human spinal cord responds effectively to the key features of this treatment. Therefore, this clinical-grade investigational device will now enable clinical trials to evaluate the safety and therapeutic efficacy of the neuroprosthetic baroreflex in the acute, sub-acute and chronic phases of SCI.

The neuroprosthetic baroreflex triggered well-controlled and reversible increases in blood pressure. Therefore, these pressor responses must be distinguished from uncontrolled, life-threatening episodes of hypertension, known as autonomic dysreflexia[42,43]. The controllability of the neuroprosthetic baroreflex alleviates the concern of triggering uncontrolled hypertensive episodes, but it remains unclear whether the long-term use of the neuroprosthetic baroreflex would not exacerbate the incidence of autonomic dysreflexia. Although future studies will need to investigate this risk, historical case studies suggest that chronic EES may instead mitigate autonomic dysreflexia[44].

In parallel, it is imperative to develop a fully implantable system that combines a paddle lead targeting the haemodynamic hotspots, a system to monitor arterial blood pressure, and a closed-loop stimulation platform to implement all the features of the neuroprosthetic baroreflex. The neuroprosthetic baroreflex foreshadows a new era in the clinical management of SCI.

Online content

Any methods, additional references, Nature Research reporting summaries, source data, extended data, supplementary information, acknowledgements, peer review information; details of author contributions and competing interests; and statements of data and code availability are available at https://doi.org/10.1038/s41586-020-03180-w.

1. Squair, J. W., Phillips, A. A., Harmon, M. & Krassioukov, A. V. Emergency management of autonomic dysreflexia with neurologic complications. *Can. Med. Assoc. J.* **188**, 1100–1103 (2016).
2. Readdy, W. J. et al. Complications and outcomes of vasopressor usage in acute traumatic central cord syndrome. *J. Neurosurg. Spine* **23**, 574–580 (2015).
3. Inoue, T., Manley, G. T., Patel, N. & Whetstone, W. D. Medical and surgical management after spinal cord injury: vasopressor usage, early surgerys, and complications. *J. Neurotrauma* **31**, 284–291 (2014).
4. Squair, J. W. et al. Spinal cord perfusion pressure predicts neurologic recovery in acute spinal cord injury. *Neurology* **89**, 1660–1667 (2017).
5. Squair, J. W. et al. Empirical targets for acute haemodynamic management of individuals with spinal cord injury. *Neurology* **93**, e1205–e1211 (2019).
6. Cragg, J. J., Noonan, V. K., Krassioukov, A. & Borisoff, J. Cardiovascular disease and spinal cord injury: results from a national population health survey. *Neurology* **81**, 723–728 (2013).
7. Wu, J.-C. et al. Increased risk of stroke after spinal cord injury: a nationwide 4-year follow-up cohort study. *Neurology* **78**, 1051–1057 (2012).

8. Illman, A., Stiller, K. & Williams, M. The prevalence of orthostatic hypotension during physiotherapy treatment in patients with an acute spinal cord injury. *Spinal Cord* **38**, 741–747 (2000).
9. Carlozzi, N. E. et al. Impact of blood pressure dysregulation on health-related quality of life in persons with spinal cord injury: development of a conceptual model. *Arch. Phys. Med. Rehabil.* **94**, 1721–1730 (2013).
10. Furlan, J. C., Fehlings, M. G., Shannon, P., Norenberg, M. D. & Krassioukov, A. V. Descending vasomotor pathways in humans: correlation between axonal preservation and cardiovascular dysfunction after spinal cord injury. *J. Neurotrauma* **20**, 1351–1363 (2003).
11. Capogrosso, M. et al. A brain-spine interface alleviating gait deficits after spinal cord injury in primates. *Nature* **539**, 284–288 (2016).
12. Wagner, F. B. et al. Targeted neurotechnology restores walking in humans with spinal cord injury. *Nature* **563**, 65–71 (2018).
13. Saadoun, S., Chen, S. & Papadopoulos, M. C. Intraspinal pressure and spinal cord perfusion pressure predict neurological outcome after traumatic spinal cord injury. *J. Neurol. Neurosurg. Psychiatry* **88**, 452–453 (2016).
14. Vale, F. L., Burns, J., Jackson, A. B. & Hadley, M. N. Combined medical and surgical treatment after acute spinal cord injury: results of a prospective pilot study to assess the merits of aggressive medical resuscitation and blood pressure management. *J. Neurosurg.* **87**, 239–246 (1997).
15. Rawlings, A. M. et al. Association of orthostatic hypotension with incident dementia, stroke, and cognitive decline. *Neurology* **91**, e759–e768 (2018).
16. Phillips, A. A., Krassioukov, A. V., Ainslie, P. N. & Warburton, D. E. R. Baroreflex function after spinal cord injury. *J. Neurotrauma* **29**, 2431–2445 (2012).
17. Phillips, A. A., Krassioukov, A. V., Ainslie, P. N. & Warburton, D. E. R. Perturbed and spontaneous regional cerebral blood flow responses to changes in blood pressure after high-level spinal cord injury: the effect of midodrine. *J. Appl. Physiol.* **116**, 645–653 (2014).
18. Courtine, G. et al. Transformation of nonfunctional spinal circuits into functional states after the loss of brain input. *Nat. Neurosci.* **12**, 1333–1342 (2009).
19. Angeli, C. A. et al. Recovery of over-ground walking after chronic motor complete spinal cord injury. *N. Engl. J. Med.* **379**, 1244–1250 (2018).
20. Gill, M. L. et al. Neuromodulation of lumbosacral spinal networks enables independent stepping after complete paraplegia. *Nat. Med.* **24**, 1677–1682 (2018).
21. Wenger, N. et al. Spatiotemporal neuromodulation therapies engaging muscle synergies improve motor control after spinal cord injury. *Nat. Med.* **22**, 138–145 (2016).
22. West, C. R. et al. Association of epidural stimulation with cardiovascular function in an individual with spinal cord injury. *JAMA Neurol.* **75**, 630–632 (2018).
23. Harkema, S. J. et al. Epidural spinal cord stimulation training and sustained recovery of cardiovascular function in individuals with chronic cervical spinal cord injury. *JAMA Neurol.* **75**, 1569–1571 (2018).
24. Harkema, S. J. et al. Normalization of blood pressure with spinal cord epidural stimulation after severe spinal cord injury. *Front. Hum. Neurosci.* **12**, 83 (2018).
25. Darrow, D. et al. Epidural spinal cord stimulation facilitates immediate restoration of dormant motor and autonomic supraspinal pathways after chronic neurologically complete spinal cord injury. *J. Neurotrauma* **36**, 2325–2336 (2019).
26. Grimm, D. et al. In vitro and in vivo gene therapy vector evolution via multispecies interbreeding and retargeting of adeno-associated viruses. *J. Virol.* **82**, 5887–5911 (2008).
27. Witten, I. B. et al. Recombinase-driver rat lines: tools, techniques, and optogenetic application to dopamine-mediated reinforcement. *Neuron* **72**, 721–733 (2011).
28. Tomer, R., Ye, L., Hsueh, B. & Deisseroth, K. Advanced CLARITY for rapid and high-resolution imaging of intact tissues. *Nat. Protocols* **9**, 1682–1697 (2014).
29. Strack, A. M., Sawyer, W. B., Marubio, L. M. & Loewy, A. D. Spinal origin of sympathetic preganglionic neurons in the rat. *Brain Res.* **455**, 187–191 (1988).
30. Capogrosso, M. et al. A computational model for epidural electrical stimulation of spinal sensorimotor circuits. *J. Neurosci.* **33**, 19326–19340 (2013).
31. Gradinaru, V., Thompson, K. R. & Deisseroth, K. eNpHR: a *Natronomonas* halorhodopsin enhanced for optogenetic applications. *Brain Cell Biol.* **36**, 129–139 (2008).
32. Phillips, A. A., Elliott, S. L., Zheng, M. M. Z. & Krassioukov, A. V. Selective alpha adrenergic antagonist reduces severity of transient hypertension during sexual stimulation after spinal cord injury. *J. Neurotrauma* **32**, 392–396 (2015).
33. Beauparlant, J. et al. Undirected compensatory plasticity contributes to neuronal dysfunction after severe spinal cord injury. *Brain* **136**, 3347–3361 (2013).
34. Minev, I. R. et al. Biomaterials. Electronic dura mater for long-term multimodal neural interfaces. *Science* **347**, 159–163 (2015).
35. Formento, E. et al. Electrical spinal cord stimulation must preserve proprioception to enable locomotion in humans with spinal cord injury. *Nat. Neurosci.* **21**, 1728–1741 (2018).
36. Cornwell, W. K. III et al. Restoration of pulsatile flow reduces sympathetic nerve activity among individuals with continuous-flow left ventricular assist devices. *Circulation* **132**, 2316–2322 (2015).
37. Purohit, S. N., Cornwell, W. K. III, Pal, J. D., Lindenfeld, J. & Ambardekar, A. V. Living without a pulse: the vascular implications of continuous-flow left ventricular assist devices. *Circ. Heart Fail.* **11**, e004670 (2018).
38. Cheng, A., Williamitis, C. A. & Slaughter, M. S. Comparison of continuous-flow and pulsatile-flow left ventricular assist devices: is there an advantage to pulsatility? *Ann. Cardiothorac. Surg.* **3**, 573–581 (2014).
39. Saleem, S. et al. Wavelet decomposition analysis is a clinically relevant strategy to evaluate cerebrovascular buffering of blood pressure after spinal cord injury. *Am. J. Physiol. Heart Circ. Physiol.* **314**, H1108–H1114 (2018).
40. Phillips, A. A., Warburton, D. E. R., Ainslie, P. N. & Krassioukov, A. V. Regional neurovascular coupling and cognitive performance in those with low blood pressure secondary to high-level spinal cord injury: improved by alpha-1 agonist midodrine hydrochloride. *J. Cereb. Blood Flow Metab.* **34**, 794–801 (2014).
41. Courtine, G. & Bloch, J. Defining ecological strategies in neuroprosthetics. *Neuron* **86**, 29–33 (2015).
42. Phillips, A. A. & Krassioukov, A. V. Contemporary cardiovascular concerns after spinal cord injury: mechanisms, maladaptations, and management. *J. Neurotrauma* **32**, 1927–1942 (2015).
43. Phillips, A. A. & Krassioukov, A. V. in *Neurological Aspects of Spinal Cord Injury* (eds Weidner, N. et al.) 325–361 (Springer International Publishing, 2017).
44. Richardson, R. R., Cerullo, L. J. & Meyer, P. R. Autonomic hyper-reflexia modulated by percutaneous epidural neurostimulation: a preliminary report. *Neurosurgery* **4**, 517–520 (1979).

[1]Center for Neuroprosthetics and Brain Mind Institute, School of Life Sciences, Swiss Federal Institute of Technology (EPFL), Lausanne, Switzerland. [2]Department of Neurosurgery, Lausanne University Hospital (CHUV) and University of Lausanne (UNIL), Lausanne, Switzerland. [3]Department of Clinical Neuroscience, Lausanne University Hospital (CHUV) and University of Lausanne (UNIL), Lausanne, Switzerland. [4]Defitech Center for Interventional Neurotherapies (.NeuroRestore), CHUV/UNIL/EPFL, Lausanne, Switzerland. [5]Department of Physiology and Pharmacology, Cumming School of Medicine, University of Calgary, Calgary, Alberta, Canada. [6]Department of Clinical Neurosciences, Hotchkiss Brain Institute, Cumming School of Medicine, University of Calgary, Calgary, Alberta, Canada. [7]Department of Cardiac Sciences, Libin Cardiovascular Institute, Cumming School of Medicine, University of Calgary, Calgary, Alberta, Canada. [8]MD/PhD Training Program, Faculty of Medicine, University of British Columbia, Vancouver, British Columbia, Canada. [9]International Collaboration on Repair Discoveries (ICORD), University of British Columbia, Vancouver, British Columbia, Canada. [10]RestoreNetwork, Hotchkiss Brain Institute, Libin Cardiovascular Institute, McCaig Institute for Bone and Joint Health, Cumming School of Medicine, University of Calgary, Calgary, Alberta, Canada. [11]Department of Neurosurgery, University of Toronto, Toronto, Ontario, Canada. [12]Department of Human Health and Nutritional Sciences, University of Guelph, Guelph, Ontario, Canada. [13]Centre for Neuroprosthetics, Institute of Microengineering, Swiss Federal Institute of Technology (EPFL), Lausanne, Switzerland. [14]Center for Biomedical Imaging, Swiss Federal Institute of Technology (EPFL), Lausanne, Switzerland. [15]Motac Neuroscience Ltd, Manchester, UK. [16]Medtronic, Minneapolis, MN, USA. [17]Department of Engineering Science and Clinical Neurosciences, University of Oxford, Oxford, UK. [18]Department of Clinical Neurosciences, University of Oxford, Oxford, UK. [19]Department of Radiology, McCaig Institute for Bone and Joint Health, University of Calgary, Calgary, Alberta, Canada. [20]Department of Emergency Medicine, Cumming School of Medicine, University of Calgary, Calgary, Alberta, Canada. [21]Faculty of Biology, University of Fribourg, Fribourg, Switzerland. [22]Institut des Maladies Neurodégénératives, Université de Bordeaux, UMR, 5293, Bordeaux, France. [23]Institut des Maladies Neurodégénératives, CNRS, UMR, 5293, Bordeaux, France. [24]These authors contributed equally: Matthieu Gautier, Lois Mahe, Jan Elaine Soriano, Andreas Rowald. [25]These authors jointly supervised this work: Grégoire Courtine, Aaron A. Phillips. ✉e-mail: gregoire.courtine@epfl.ch; aaron.phillips@ucalgary.ca

Methods

Animal models

Experiments were conducted on adult female Lewis rats (180–220 g body weight, 14–30 weeks of age) and adult male or female TH-Cre rats (180–400 g body weight, 14–30 weeks of age)[27]. Housing, surgery, behavioural experiments and euthanasia were performed in compliance with the Swiss Veterinary Law guidelines. Animal care, including manual bladder voiding, was performed twice daily for the first 2 weeks after injury and once daily for the remaining period after injury[45]. Procedures and surgeries were approved by the Veterinary Office of the Canton of Geneva (Switzerland; GE/87/17 and GE/212/17) and the University of Calgary (AC17-0185). Non-human primate experiments were approved by the Institutional Animal Care and Use Committee of China Academy of Medical Sciences in Beijing (LQ19003) and performed in accordance with the European Union directive of 22 September 2010 (2010/63/EU) on the protection of animals used for scientific purposes in an AAALAC-accredited facility (Chinese Academy of Science, Beijing, China), as previously described[11]. Three healthy male rhesus monkeys (*Macaca mulatta*) aged 5 years old, and weighing 5.4, 5.4 and 5.8 kg, were housed individually in cages designed according to European guidelines (2 m × 1.6 m × 1.26 m). Environmental enrichment included toys and soothing music.

Rodent anaesthesia use

All non-terminal experiments were conducted by anaesthetizing animals with isoflurane (initial induction 5% and maintained on a Bain's system at 2%). Terminal electrophysiological assessments were carried out as previously described[46] four weeks after SCI. In brief, animals were anaesthetized with urethane (1.5 g kg^{-1}; intraperitoneally) and core body temperature was maintained at 37 °C using a self-regulating heated pad connected to a rectal probe. Depth of anaesthesia was continually monitored by assessing withdrawal reflexes and respiratory rate.

Surgical procedures and post-surgical care

Spinal cord injuries. Rodent spinal cord injuries were performed according to our previously published work[47,48]. In brief, a laminectomy was performed on the TIII vertebra to expose the T3 spinal segment. Following this the rat was transferred to the Infinite-Horizons (IH-0400 Impactor, Precision Systems and Instrumentation LLC) impactor[49] stage, where the TII and TIV spinous processes were securely clamped using modified Allis forceps[47]. The rat was stabilized on the platform and the impactor tip (2.5 mm) was properly aligned using a three-dimensional coordinate system moving platform. The IH system was set to deliver an impact force of 400 kdyn, with a 5 s dwell time[47]. Analgesia (buprenorphine, Essex Chemie AG, 0.01–0.05 mg per kg, subcutaneously) and antibiotics (amoxicillin 200 mg per 4 ml, Sandoz, 200 mg l^{-1} ad libitum) were provided for 3 and 5 days after surgery, respectively. Bladders were manually expressed for approximately one week, after which time animals regained reflexive voiding[45,47].

For non-human primate experiments, all the surgical procedures were terminal. Monkeys were fasted for 12 h before anaesthesia to minimize the risk of vomiting and aspiration. Monkeys were first aseptically prepared and anaesthetized with ketamine (10 mg kg^{-1}, intramuscular injection) and propofol (6 mg kg^{-1} loading followed by maintenance at 0.3 mg kg^{-1} min^{-1} via an intravenous line). Monkeys were then intubated and put the tested animal on the surgery table. Ketamine and propofol were complemented with isoflurane (1–3%). Hydration was maintained through intravenous fluids at 5–10 ml kg^{-1} h^{-1}. Temperature was maintained using heating blankets and a warmed table. A certified functional neurosurgeon (J.B.) supervised all the surgical procedures. The complete experiment for each animal was performed during a single operation lasting less than 12 h. All three monkeys received a spinal cord injury. A partial laminectomy was made at the level of the T2/T3 thoracic vertebrae. The spinal cord was compressed for 30 s and then transected at the T3 segment. At the end-point of the experiment, monkeys were further anaesthetized (already in the surgical plane of anaesthesia from the previous procedure) with an intramuscular injection of ketamine (15 mg kg^{-1}) followed by intravenous pentobarbital (100–150 mg kg^{-1}) until cessation of breathing.

Epidural electrical stimulation implants. For positioning epidural stimulation electrodes in rats, targeted epidural spinal stimulation (EES) was delivered in three modes, as previously described[18,21,34,48,50]: (1) using a stereotax for functional mapping experiments, (2) with electrodes sewn to the dura[18,21,48,50], and (3) using e-dura technology[34]. For functional mapping, a Teflon-coated stainless-steel wire (AS632, Cooner Wire) was fixed to a stereotax to allow stable placement of the electrode while mapping all spinal segments. Laminectomies were performed starting at L2, and moving rostral. Stimulation was provided at 50 Hz, with a pulse length of 2 ms, and the current increased from 0 to approximately 200 mA. Upon visible motor threshold, the stimulation was stopped. For terminal experiments targeting haemodynamic hotspots, a partial laminectomy was performed over T11–T13 spinal segments, or over the L2 spinal segment. Stimulating electrodes were created by removing a small part of the insulation (approximately 400 μm notch) from Teflon-coated stainless-steel wires (AS632, Cooner Wire), which were subsequently secured at the midline by suturing the wires to the dura. A common ground wire (approximately 1 cm of Teflon removed at the distal end) was inserted subcutaneously. Stimulation in these cases was driven by an external stimulator (A-M Systems). To insert and stabilize e-dura implants into the epidural space two partial laminectomies were performed at vertebrae levels L1–L2 and T8–T9 to create entry and exit points for the implant. The implant was gently pulled above the dura mater using a surgical suture[34]. Electrophysiological testing was performed intra-operatively to fine-tune positioning of electrodes. The connector of the implant was secured into a protective cage plastered using freshly mixed dental cement on top of the L2–L3 vertebra. Stimulation was then delivered through an IZ2 stimulator (Tucker-Davis Technologies; see 'Closed loop haemodynamic monitoring platform and control policies'[21]).

Dorsal rhizotomy. Under urethane anaesthesia, a laminectomy was performed to expose the T11–T13 posterior roots. The laminectomy was laterally expanded to expose the dorsal root ganglia. The posterior roots were systematically cut bilaterally using microscissors. This procedure was completed in the presence of either T12 or L2 EES (Extended Data Figs. 3, 4).

Splanchnic ganglia manipulations. For experiments involving manipulation of the splanchnic ganglia, a midline laparotomy was performed. The hepatic portal vein, inferior vena cava, and abdominal aorta were gently retracted. The surrounding fascia was bluntly dissected to expose the coeliac, superior mesenteric, and inferior mesenteric ganglia. At this point either stimulation was applied (see 'Rodent electrophysiology') or an axotomy was performed to sever the connection from the spinal cord to the ganglia.

Haemodynamic and sympathetic nerve activity monitoring. We recorded blood pressure and sympathetic nerve activity chronically (Extended Data Figs. 1, 2) using wireless telemeters (TRM56SP SNA and Pressure Telemeter, Kaha Sciences). A midline abdominal incision was made to expose the peritoneal cavity, followed by a blunt dissection to reach the descending aorta. The aorta was temporary occluded using a 4-0 silk, one to two millimetres rostral to the iliac bifurcation. The pressure sensor was inserted in the aorta so that the tip was just caudal to the renal artery, and fixed with a surgical mesh and biocompatible surgical glue. After catheterization of the aorta, the renal nerve was exposed immediately caudal to the right kidney. A micro electrode wire was sutured to the renal nerve using 8-0 silk sutures (Ethicon), and

the ground was left freely in the peritoneal cavity. The quality of SNA recordings was assessed weekly. Because conventional approaches, such as exposure to stress-evoking high-frequency noise, could not be used in rats with complete SCI, we devised a new paradigm based on the recruitment of afferents below the level of injury. We pinched the tail to evoke a noxious stimulus that triggered activity in the nerve recording. For each rat, we ensured that the signal remained stable and responsive. Analgesia (buprenorphine, Essex Chemie AG, 0.01–0.05 mg per kg, subcutaneously) and antibiotics (amoxicillin 200 mg per 4 ml, Sandoz, 200 mg l^{-1} ad libitum) were provided for 3 and 5 days after surgery, respectively. In some cases, a carotid catheterization was used for terminal experiments. In brief, after induction of anaesthesia, the hair on the neck was shaved, and the surgical site cleaned with alcohol and betadine. The right common carotid artery was exposed and isolated from the internal jugular vein using blunt dissection. The carotid artery was then permanently occluded rostrally and temporarily occluded caudal to the implantation site using 4-0 silk sutures. A small incision was made in the artery wall using a bent tip 20-gauge needle and the blood pressure device guided into the lumen and advanced caudally to approximately 5–6 mm rostral to the aortic arch. The catheter was then secured with two 4-0 silk sutures[47].

For non-human primates, a large-animal catheter (AD Instruments, MPR-500; 5F) was inserted into the subclavian artery according to the same surgical procedures described above. In all cases, for rodents and non-human primates, data were collected, analogue-to-digital converted (PowerLab; AD Instruments), and sampled at 1,000 Hz (LabChart; AD Instruments).

Intravenous lines. Rodent intravenous drug delivery was performed via a femoral venous line. For non-human primate experiments, propofol and required fluid management was delivered intravenously via a dorsal venous arch line.

Implementation of a simulated orthostatic challenge in rodents and non-human primates

A custom-made servo-controlled lower body negative-pressure (LBNP) chamber was manufactured to induce a controlled reduction of arterial pressure in rodents (Extended Data Fig. 1). Animals were placed inside a sealed rectangular prism (dimensions: 25.5 cm long, 14 cm wide, 13 cm height) from the feet up to the xiphoid process in the prone position. Negative pressure was induced using a vacuum pump attached to an electro-pneumatic regulator (SMC series ITV2000-Q) that allowed precise control of the pressure inside the chamber. Analogue output of the chamber pressure from the regulator was fed through a DAQ USB device (NI USB-6001) to a computer running LabView. Using the same DAQ connection, custom software was developed to induce preset pressure changes, and the pressure in the chamber is monitored in a closed loop to ensure a constant orthostatic stimulus. Using this approach, we found that a stimulus of −10 mmHg led to a reproducible drop in haemodynamics that uninjured animals could recover from, but were unable to respond to after SCI (Extended Data Fig. 2h–j).

For non-human primates, we custom-built a larger LBNP system (Extended Data Fig. 9, step 6). To create a negative-pressure environment inside the LBNP chamber a 3-stage 120 V AC (368 W) vacuum motor (Model 116565-13, AMETEK-Lamb Electric) with a 145 mm diameter compressor housing (38 mm diameter inlet) and 48mm diameter exhaust was used. The vacuum motor was regulated by an AC variable motor speed control (model KBWC-115K, KB Electronics) to vary the frequency cycle of the vacuum motor and manipulate the vacuum pressure produced. Vacuum pressure was measured via 5 mm polyurethane tubing that ran from the LBNP chamber interior to a dual-port on-chip 4 pin pressure sensor (Model MPX2050DP, NXP Semiconductors) which produced an analogue signal (mV) integrated by a PCB-ADC board. The converted values in mmHg were displayed via an LCD display (model DMS-20LCD-0-5B-C, Murata Power Solutions). The analogue reading from the pressure sensor was also wired from the PCB carrying the analogue pressure signal to be recorded and visualized in parallel with physiological metrics via the Powerlab (PowerLab, AD Instruments) and LabChart software (LabChart, AD Instruments). A linear power supply (Model IHBB512, International Power) was used to convert the 120 V AC input to a 12 V DC output (1.2 A) to provide the appropriate voltage to the pressure sensor, LCD display, and a brushless air exchange fan. The components were mounted and secured in an aluminium chassis, which was framed with acrylic plexiglass panels to form the vacuum unit. A 120 mm DC brushless fan (model OD1238-12HSS, Orion Fans) was used to exhaust warm air from the interior of the vacuum unit during operation. The vacuum unit was attached to the LBNP chamber via 2.75 m (30 mm diameter) of flexible PVC Schedule 40 tubing. The ends of the tubing were fitted with reducing couplers (42 mm OD to 30 mm ID). The vacuum end was secured to a custom housing on the base of the vacuum unit which connected the vacuum intake port with a 43 mm (ID) PVC coupler. The chamber end was connected via a 43 mm (ID) female end, which was coupled to a 30 mm (OD) × 20 mm NPT male stud threaded into the base of the LBNP chamber and secured with adhesive to prevent any leaks. The exterior body of the LBNP chamber was made from polyethylene, structurally supported by an interior frame made from 32 mm diameter PVC piping. A custom nylon cover was fitted around the chamber, and extended approximately 0.5 m from the top of the chamber. After placement of non-human primates in the chamber, the animal was secured and an airtight seal created. To ensure consistent positioning of the monkeys during negative pressure, a custom seat with an adjustable range of approximately 240 mm was manufactured from 32 mm (diameter) PVC piping, and was secured to the interior frame via a PVC tee joint.

Visualization of the anatomical features of the thoracic spinal cord

Microcomputed tomography in rodents. Repeated imaging of the thoracic spinal column was conducted using the microcomputed tomography scanner Skyscan 1076 (Bruker μCT), as previously described[21]. The resulting projection images were reconstructed into 3D renderings using NRecon and GPURecon Server (Bruker μCT). Segmentation and 3D models were constructed with Amira (FEI Vizualisation Sciences Group). The shape of vertebrae was measured using microcomputed tomography imaging. The spinal cords of one rat was imaged, and the entire bone structure was reconstructed in 3D. The 3D renderings were exported in the virtual reality modelling language file format WRL that was later merged with spinal tissue and dorsal root reconstructions.

Magnetic resonance imaging in rodents. The rodent's spinal cord was imaged post mortem in a 9.4T MRI system (Magnex Scientific), equipped with 400 mT m^{-1} gradients and interfaced to a DirectDrive console (Varian) using a custom-made volume quadrature radio frequency coil. High-resolution images of the spinal cord were acquired using a multi-slice fast-spin-echo sequence (TE/TR = 12.5/5,000 ms, echo train length = 4) yielding 0.1 × 0.1 mm^2 in-plane resolution and 120 1-mm slices covering the entire cord.

Measurements of spinal segment morphologies on fresh tissue. For each subject (n = 3 rodents; n = 3 non-human primates), the spinal segments were identified on the basis of the innervation of the dorsal roots. The centre of the segment was defined as the entry point of the rootlets. After measuring the length of vertebra and the relationships between vertebra and spinal segments, the entire spinal cord was extracted and the roots moved perpendicular to the spinal cord to clearly visualize the segments. The location and length of each segment was then calculated.

Design, fabrication and characterization of soft electrode arrays, e-dura

The implant manufacturing follows the silicone-on-silicon process, enabling wafer-scale fabrication and the design freedom required to

produce devices adapted for both rat and non-human primate models. In brief, electrode arrays were fabricated in a class 100 cleanroom environment by embedding thin-film gold tracks between two layers of silicone rubber (polydimethylsiloxane, PDMS, Sylgard 184, Dow Corning) to form stretchable interconnects[34]. The top silicone layer includes vias that define active stimulation sites, through which a soft composite coating is screen printed onto the gold. The coating material is fabricated by dispersing meso-scale platinum particles (Strem Chemicals, 0.27–0.47 μm average size) within a PDMS matrix, to create a conductive paste that offers a balance between the charge transfer properties of platinum, a roughened surface for increased equivalent area and the mechanical properties of PDMS.

Two different six-polar implant layouts were used for rats and non-human primate models, with dimensions adapted to the different anatomical scales. Electrodes were designed with a circular shape (500 μm diameter) for rats and rectangular (0.7 mm by 2 mm) for non-human primates. The resulting geometric surface areas (GSA) for the two designs are about 0.002 cm^2 and 0.014 cm^2, respectively. The total device thickness was about 100 μm for rat implants and 400 μm for non-human primate implants, in accordance with the dimensions of the vertebral columns for each species. Devices were sterilized using ETO.

Rat implants were connected via stainless steel wires (Cooner Wire) to 12-contact Omnetics Micro 360 connectors (6 used as stimulation channels connected to the separate electrodes on the array, and 6 as stimulation ground in vivo). Non-human primate implants were connected to standard 8-polar implantable leads.

Before implantation, the arrays were characterized in vitro by acquiring electrochemical impedance spectra (EIS) of the electrodes in PBS solution (Gibco PBS, pH 7.4, 1×), using a platinum wire as a counter electrode and an Ag|AgCl reference electrode (Metrohm, El. Ag/AgCl DJ RN SC: KCl). In this three-electrode configuration, EIS measurements were taken at room temperature using a Gamry Instruments Reference 600 potentiostat (100 mV amplitude, 1 Hz–1 MHz frequency).

Virus production

Viruses used in this study were acquired commercially. The following virus was obtained for tract tracing: AAV-DJ-hSyn-flex-mGFP -2A-synaptophysin-mRuby (Stanford Vector Core Facility, reference AAV-DJ-GVVC-AAV-100, titre 1.15×10^{12} genome copies (GC) per ml[26]). Optogenetics experiments were carried out using AAV5-EF1a-dio-eNpH R3.0-RFP-WRPE[31] (v203-5 from Viral Vector Faciltiy VVF, Neurosciences Center Zurich (ZNZ); titre 5.6×10^{12} viral genomes (VG) per ml), AAV5-CAG-eNpHR3.0-eYFP[31] (Gene Therapy Center Virus Vector Core Facility, The University of North Carolina; titre 6×10^{12} VG per ml), and AAV5-Ef1a-DIO-hChR2 (H134R)-eYFP (Gene Therapy Center Virus Vector Core Facility, The University of North Carolina; titre 4×10^{12} VG per ml). AAV5 production was carried out in HEK293-AAV cells (Agilent) and purified using an iodixanol gradient and ion-exchange chromatography according to standard procedures, yielding vector suspensions with the following titres: AAV5-CMV-Cre (1.12×10^{12} VG per ml). All flexed AAV vectors used in the present study showed transgene expression only upon Cre-mediated recombination. Injection volumes, coordinates and experimental purpose using these viruses are described specifically below. Pseudorabies tracing was completed using Bartha strain PRV152 (expressing GFP; 4.9 × 109 pfu per ml, Princeton University).

Viral injections

Brainstem injections were performed by stereotaxic injections using high-precision instruments under isoflurane anaesthesia. All anterograde tract-tracing and optogenetic experiments manipulating RVLM neurons were performed in TH-Cre rats[27]. A craniotomy was performed bilaterally over the brainstem medulla oblongata and AAV-DJ-hSyn-flex-mGFP-2A-synaptophysin-mRuby (titre 1.15×10^{12} GC per ml[26]) was injected into the RVLM. Four injections (250 nl per injection) at two different rostrocaudal locations at two depths were made bilaterally. Coordinates used for targeting this nucleus were −12.12 to −12.62 mm anteroposterior from bregma, 2 mm lateral and 7.8 to 8 mm ventral from the surface of the cerebellum[51]. Injections were performed using the Hamilton injection system. Viruses were injected and the needle was held in place for 2 min before being slowly retracted[48]. For splanchnic ganglia injections, a midline laparotomy was performed. The hepatic portal vein, inferior vena cava, and abdominal aorta were gently retracted. The surrounding fascia was bluntly dissected to expose the coeliac, superior mesenteric, and inferior mesenteric ganglia. Viruses were injected at 0.2 μl per minute using glass micropipettes connected via high pressure tubing (Kopf) to 10-μl syringes under the control of microinfusion pumps. After injection of the tracer, the abdominal muscle wall and skin were closed with 5-0 monocryl and 5-0 prolene sutures, respectively. Dorsal root ganglia injections were completed by exposing the T12 dorsal root ganglia with a laminectomy. Viruses were injected under stereotaxic guidance at 0.2 μl per minute using glass micropipettes connected via high pressure tubing (Kopf) to 10-μl syringes under the control of microinfusion pumps.

Fluorogold tracing

Fluorogold 0.4% in distilled water (fluorochrome) was injected into either the splanchnic ganglia (2 μl) or the intraperitoneal cavity (100 μl) 7 days before perfusion[52].

Rodent electrophysiology

For stimulation of the rostral ventrolateral medulla and splanchnic ganglia, a tungsten bipolar concentric electrode was positioned either in the rostral ventrolateral medulla (coordinates: −12.12 to −12.62 mm anteroposterior from bregma, 2 mm lateral and 7.8 to 8 mm ventral from the surface of the cerebellum) or immediately on top of the splanchnic ganglia. Three silver ball electrodes were used to record any evoked activity from the surface of the exposed spinal cord at various locations (over the T11, T12 and T13 roots), as we have previously described for other contexts[46]. Stimulation was delivered in 200 μs square wave pulses at the maximum amplitude possible before large motor responses were evoked (typically between 600 μA and 800 μA) and at a frequency of 1 Hz using a STG 4004 stimulus generator (Multi Channel Systems). Evoked activity was amplified and recorded using an A-M systems differential amplifier, PowerLab and LabChart Pro acquisition and analysis system (AD Instruments). For analysis, 100 action potential traces from each recording site were averaged and the peak to peak delay of the evoked potential was quantified.

Optogenetics experiments

Animals were anaesthetized with urethane (see 'Rodent anaesthesia use') to preserve spinal reflexes during the experiment. A carotid catheterization was first performed to record blood pressure and a monopolar electrode was fixed to the T12 segment for epidural stimulation. A laser was secured to a stereotax, and positioned directly over top of either the splanchnic ganglia (Extended Data Fig. 5). Systolic, diastolic, and mean arterial pressure were then derived on a beat-by-beat basis over 10 min to establish resting haemodynamics. Once resting haemodynamics were established, EES was then delivered at 50 Hz, with a pulse length of 2 ms, and the current increased from 0 to approximately 200 mA. Upon visible motor threshold, the stimulation was stopped. Once the appropriate amplitude for stimulation was established, trials were performed by taking 30 s of haemodynamic baseline, followed by 10 s of stimulation alone and 30 s of laser combined with stimulation. A laser (Laserglow, 589 nm Yellow DPSS Laser System) transmitted yellow light through an optic fibre (200 μm core diameter, 0.22 NA, Thorlabs) that was held in a 1.25-mm ferrule at the surface of the ganglia. Light stimulation was delivered over 10 s and consisted of 10-ms-long pulses delivered at 40 Hz[48]. After completion of the experiment, the animal was overdosed with urethane. The coeliac ganglia were dissected and postfixed.

For optogenetic manipulation of the rostral ventrolateral medulla, optic fibres were implanted immediately after virus injection (see 'Viral injections') in the right and left RVLM using the coordinates previously described (−12.6 mm anteroposterior, 2 mm lateral, −7.8 mm ventral). The ferrule was fixed with dental cement. Light was transmitted to the brain through a ferrule-to-ferrule connection cable[48]. Laser pulses were driven by an external stimulator (A-M Systems) to ensure precise control of stimulation features. Light stimulation was delivered over 10 s and consisted of 10-ms-long pulses delivered at 40 Hz[48]. Experiments were completed under urethane anaesthesia with blood pressure monitoring in place.

Pharmacological experiments

For pharmacological experiments drugs were infused as a bolus through an intravenous line. Doses were determined based on pilot experiments and in vivo experimental confirmation. Drug doses included sodium nitroprusside: 10 μg kg^{-1}, and prazosin: 10 μg kg^{-1}.

Hybrid computational model of the rat spinal cord

We previously developed and validated experimentally a hybrid computational model of EES of the lumbar and sacral regions of the rat spinal cord[11,30]. We extended this effort to create a hybrid computational model of the lower thoracic and upper lumbar segments of the rat spinal cord. For this purpose, we acquired high-resolution MRI datasets of the rat spinal cord and manually segmented the white matter, spinal roots, cerebrospinal fluid (CSF) and vertebral bone to create a realistic 3D reconstruction of the thoracic and lumbar spinal cord of a rat. We artificially filled the epidural space between the bone and CSF and assigned it as the material epidural fat. In addition, we used tracings of the grey matter of rats and scaled them to the size of the white matter to create this material. We then placed this model in a large saline conductor to represent the remaining body of the rat. We assigned the same conductivity values as previously to this model[30] and calculated the electric fields elicited by electrical spinal cord stimulation using a finite element approach. The models were all implemented in Sim4Life v3.4 (ZMT Zürich MedTech AG)[36].

Furthermore, we combined these solutions with anatomically and biophysically realistic neural structures to derive the type of fibres and neurons activated by the stimulation[53,54]. We then coupled these activation maps with a purely hypothetical network model composed of integrate-and-fire neurons that connected to an approximation of pre-ganglionic neurons. Three network architectures were tested. The connection was mediated through either monosynaptic, disynaptic excitatory, or disynaptic inhibitory pathways. Electrophysiological parameters were recorded in silico at all neuron populations.

Hybrid computational model of the human spinal cord

We repeated the same procedure as in 'Hybrid computational model of the rat spinal cord' with MRI and computed tomography datasets of a human patient implanted with the MDT 5-6-5 array. We identified optimal multipolar stimulation parameters by using a genetic algorithm to target the lower thoracic spinal roots[30].

Closed loop haemodynamic monitoring and stimulation platform and control policies

Our closed loop monitoring and control platform was implemented within a multi-threaded C++ code (Visual Studio 2010, Microsoft) running on a quad-core Microsoft Windows 7 computer. Stimulation patterns were applied via an RZ5 processing unit (Tucker-Davis Technologies) connected to an MS16 Stimulus Isolator (Tucker-Davis Technologies)[21]. The integrated haemodynamic recording system generated a raw blood pressure trace, which was imported into the C++ environment in (soft) real-time through the accompanying DAC on the RZ5 processing unit. The control logic delivered stimulation to electrodes based on the trajectory of mean blood pressure or the sum firing rate derived from the RVLM. Control algorithms continuously calculated the deviation of blood pressure from the mean. The change in amplitude for electrode configuration was continuously adjusted and scaled according to a proportional and an integral coefficient. This continuous control was further modulated by key biomimetic features. Specifically, our electrode array consists of paired electrodes at three key haemodynamic hotspots. Therefore, we integrated a biologically- elevant delay (2.5 ms) between each segment, in line with conduction delays that were experimentally tested (Extended Data Fig. 6). Furthermore, to re-integrate the frequency dynamics lost after SCI (Fig. 3, Extended Data Fig. 6), we continuously adjusted the amplitude of stimulation between 90% and 100% at the relative frequency of Meyer waves in each species (for example, rat: 0.4 Hz, non-human primate: 0.1 Hz; human: 0.1 Hz). Stimulation was then delivered using an IZ2 stimulator (Tucker-Davis Technologies) to stimulation arrays. This custom control software therefore delivered all the key components of the biomimetic stimulation. Custom-developed C++ and Tucker-Davis Technologies codes can be made available through material transfer agreement upon reasonable request.

For non-human primate experiments, EES was delivered using clinical grade technologies ($n = 3$). Stimulation was delivered with an IPG (Medtronic Activa RC) that enabled monopolar and multipolar stimulation at constant current or constant voltage through one or a subset of the 6 electrodes of the custom designed non-human primate array or the case of the IPG (anode). The IPG was modified from its clinical version with an investigational firmware that enabled real-time communication with a software running on an external computer (NEUWalk Research Programmer Application NRPA, Model 09103, Medtronic[11]). The NRPA acted as a relay between EES triggering commands sent by the control software (conceptually described above), which we implemented in a compatible Python package and accompanying C# interface. It communicated wirelessly with the IPG through the following communication chain: the NRPA sent commands via a virtual COM port corresponding to a Bluetooth adaptor, which received this command and forwarded it to a virtual COM port 6 corresponding to a USB adaptor, a USB to infrared adaptor (ACT-IR224UN-LN115-LE, ACTiSYS Corporation) transformed this command into infrared signals that were then read by a modified Medtronic patient's programmer (Sensing Programmer Telemetry Module SPTM, Medtronic), which finally transmitted the command to the IPG by electromagnetic induction through the skin (Extended Data Fig. 8). Thus, our custom control software interacted with this clinical grade stimulation in a closed loop, while also delivering all the key components of the biomimetic stimulation, including delays between each of the three segments as well as a 0.1 Hz overlay to ensure the dynamics of the system were recapitulated.

Rodent perfusion protocol

For all rodent perfusions, animals were anaesthetized by an intraperitoneal injection of 0.5 ml Pentobarbital-Na (50 mg ml^{-1}; PBS) and transcardially perfused with approximately 80ml Ringer's solution containing 100,000 IU l^{-1} heparin (Liquemin, Roche) and 0.25% $NaNO_2$ followed by 300 ml of cold 4% phosphate buffered paraformaldehyde (PFA), pH 7.4. The tissue was removed and postfixed in the same fixative before they were transferred to 30% sucrose in phosphate buffer for cryoprotection, or placed in PBS before tissue clearing[48]. Before cryosectioning, tissue was embedded in Tissue Tek O.C.T (Sakura Finetek Europe B.V.) and frozen at −80 °C.

Tissue clearing and imaging of rat brainstem and spinal cord

Rat brainstem and spinal cord were cleared using uDISCO[55] and CLARITY[56], respectively, four weeks after injection of AAV-DJ-hSyn-flex-mGFP-2A-synaptophysin-mRuby[26]. Rats were perfused transcardially first with 0.1 M PBS followed by 4% PFA (in 0.1 M PBS, pH 7.4) at 4 °C. The rat brainstem (to visualize the rostral ventrolateral medulla injection site) and thoracic spinal cord (to visualize the contusion lesion) were

dissected and postfixed in 4% PFA (in 0.1 M PBS) for 24 h at 4 °C. The dura was removed from the samples before clearing.

uDISCO clearing of rat brainstem. uDISCO clearing of the rat brainstem was initiated by stepwise dehydration in increasing concentrations of tert-butanol dissolved in dH_2O with a total volume of 5 ml at 35 °C as follows: 30% tert-butanol overnight, 50% for 10 h, 70% overnight, 80% for 10 h, 90% overnight, 96% for 10 h, and 100% overnight. The sample was then incubated in 5 ml of dichloromethane at room temperature for 70 min with shaking. This was then followed by incubation in BABB-D4 (BABB: 2:1 mixture of benzyl benzoate to benzyl alcohol; 4:1 mixture of BABB to diphenyl ether; 0.4% v/v vitamin E) for 24 h at room temperature before imaging.

CLARITY clearing of rat spinal cord. To initiate CLARITY of the rat spinal cord, the sample was incubated in A4P0 hydrogel solution (4% acrylamide in 0.001 M PBS with 0.25% of the photoinitiator 2,2′-azobis[2-(2-imidazolin-2-yl)propane] dihydrochloride (Wako Pure Chemical)) for 24 h at 4 °C with gentle nutation. The sample was then degassed by bubbling nitrogen gas through the tube for 3 min then quickly and tightly closing the tube cap. Hydrogel polymerization was then initiated by incubating the sample in a 37 °C water bath for 2 h. Excess hydrogel was removed, and tissue was washed in 0.001 M PBS for 5 min at room temperature. The sample was then placed in the X-CLARITY Tissue Clearing System I (Logos Biosystems) set to 1.2 A, 100 rpm, 37 °C. Clearing solution was made in-house and consisted of 40 g of sodium dodecyl sulfate (SDS), 200 mM boric acid, and filled to a total volume of 1 l with dH_2O (pH adjusted to 8.5). The sample was cleared after about 10–15 h. After clearing, the sample was washed for at least 24 h at room temperature with shaking in 1× PBS and 0.1% Triton X-100 (with 0.02% sodium azide) to remove excess SDS. The sample was then incubated in RIMS (40 g of Histodenz dissolved in 30 ml of 0.02 M phosphate buffer, pH 7.5, 0.01% sodium azide, refractive index 1.465) for at least 24 h at room temperature with gentle shaking before imaging.

Imaging was performed using a custom-built CLARITY-optimized light-sheet microscope (COLM) as described previously[28]. A customized sample holder was used to secure the brainstem or spinal cord sample in a chamber filled with BABB-D4 (uDISCO) or RIMS (CLARITY). Samples were imaged using a 10× (injection site) or 4× (lesion) objective with two lightsheets illuminating the sample from the left and the right sides. The pixel resolution for the 10× acquisition was 0.48 × 0.48 × 3 µm and 1.4 µm by 1.4 µm by 5 µm for the 4× acquisition in the *x*-, *y*- and *z*-directions. Images were acquired as 16-bit TIFF files and reconstructed in 3D using TeraStitcher[57]. 3D reconstructions of the raw images were produced using Imaris (Bitplane, v.9.0.0). The spinal cord lesion reconstructions were performed manually using Imaris.

Immunohistochemistry

Immunohistochemistry was performed according to the following procedures[48]. First, sections were thawed for one hour at room temperature. Next, sections were rehydrated in PBS for 10 min. Normal donkey serum (Millipore) was then placed on the slides for 30 min. Lastly, primary antibodies (350 µl) were placed on the sections and allowed to incubate overnight. The following primary antibodies were used: guinea pig anti-neuronal nuclei (NeuN, 1:300, Millipore, ABN90P), rabbit anti-cFos (FOS, 1:500, Calbiochem, PC38), mouse anti-tyrosine hydroxylase (TH, 1:2,000, Millipore, MAB318), mouse anti-glial fibrillary acidic protein (GFAP, 1:1,000, Sigma-Aldrich, G3893), mouse anti-vesicular glutamate transporter 1 (VGLUT1, 1:1,000, Millipore, MAB5502), rabbit anti-ChAT (1:50, Millipore, AB144P) and rabbit anti-α_1 adrenergic receptor (ADRA1, 1:500, Abcam, AB3462). Secondary antibodies included: Alexa Fluor 647 Donkey Anti Mouse (1:200; Life Technologies, A31571), Alexa Fluor 488 Donkey Anti Rabbit (1:200, Life Technologies, A21206), Alexa Fluor 488 Goat Anti Rabbit (1:200, Life Technologies, A11008), Alexa Fluor 555 Goat Anti Rabbit (1:200, Life Technologies, A21428), Alexa Fluor 555 Goat Anti Guinea Pig (1:200, Life Technologies, A21435) and also DAPI (1:1,000, Life Technologies). Following the secondary staining, three additional washes with PBS were performed and a Nissl stain was applied (1:100, Millipore). Immunofluorescence was imaged digitally using a slide scanner (Olympus VS-120 Slide scanner) or confocal microscope (Zeiss LSM880 + Airy fast module with ZEN 2 Black software (Zeiss)). Images were digitally processed using ImageJ (ImageJ NIH) software or Imaris (Bitplane, v.9.0.0).

Fluorescence in situ hybridization

Interneurons trans-synaptically connected to splanchnic ganglia were examined for co-localization of *Slc17a6* mRNA using the RNA labelling kit from Molecular Instruments. After perfusion, tissues were fixed in 4% phosphate buffered paraformaldehyde for 3 h at 4 °C before they were transferred to 30% sucrose in phosphate buffer for cryoprotection at 4 °C for two nights. RNA in situ hybridization was performed on 40-µm spinal cord sections. Samples were placed in 5× SSCT (20× SSC buffer, Invitrogen; 10% Tween 20, Applichem) for 10 min and then pre-hybridized in 30% probe hybridization buffer (Molecular Instruments) for 30 min at 37 °C. Samples were hybridized overnight at 2 µM probe concentration in 30% probe hybridization buffer at 37 °C. After hybridization, samples were washed in a solution of 30% probe wash buffer (Molecular Instruments) and 5× SSCT four times 15 min. Sections were then incubated in an amplification buffer (Molecular Instruments) for 30 min at room temperature. In the meantime, fluorophore-labelled HCR hairpins (Molecular Instruments) were snap-cooled (heating at 95 °C for 90 s) and cooled down to room temperature. Amplification was performed overnight at room temperature at a concentration of 120 nM per hairpin in the amplification buffer. After amplification, samples were washed in 5× SSCT for at least twice for 30 min to remove unbound hairpins. Lastly, sections were air-dried and cover slipped using Mowiol (Calbiochem).

Haemodynamic analyses

Classical orthostatic challenge using a tilt test. Baseline values for haemodynamics (that is, systolic blood pressure, mean arterial pressure, and diastolic blood pressure) were recorded over 5 min. Next, rats ($n = 4$) were tilted 90° upright while secured to a platform for 3 min to maximally challenge animals against gravitational forces. Delta values were calculated compared to baseline for each animal, for each minute (Extended Data Fig. 1).

Response to spinal cord injury. Resting systolic, diastolic and mean arterial blood pressure, as well as heart rate, were assessed over a 10-min period before spinal cord contusion (Extended Data Fig. 2). After this period, the experimenter initiated the Infinite-Horizons impactor (rodent) or forceps compression (non-human primate). The severity of the response to spinal cord contusion was assessed as the maximum change in blood pressure (systolic, diastolic and mean taken independently) and sympathetic nerve activity (rodent only) over the next 1-min period. The resulting neurogenic shock was then quantified as the minimum blood pressure (systolic, diastolic and mean taken independently) and sympathetic nerve activity (rodent only) after 1 h.

Establishment of haemodynamic instability after spinal cord injury. Our comprehensive chronic analysis pipeline is predicated on generating an entirely automated analysis. Therefore, every aspect of the following methods requires no human intervention. First, we calculated systolic, blood pressure, diastolic blood pressure, mean arterial pressure, and heart rate on each hour of data (save automatically). At this step we filtered out non-physiological values (filter set with a heart rate of fewer than 180 beat per min (bpm) or greater than 625 bpm), then saved the detailed record of blood pressure for further analysis. Next, we removed outliers by binning each outcome in intervals of ten seconds, and computing the first principal component

eigenvalue. We then performed hierarchical clustering ($k = 2$) to identify and remove remaining outliers. Next, we extracted the raw sympathetic nerve activity recordings. We first applied a second order Butterworth filter (100–500Hz) and rectified the signal. We then computed a ten millisecond windowed integral (that is, 'iSNA'). Background levels of iSNA were measured in a post-mortem animal and subtracted from the final values. With our final dataset, we then used a local polynomial regression to interpolate missing data points (for example, during animal care). Data were then summarized hourly to generate a total of 1,176 (24 h and 7 weeks of data collection) data points per animal. We determined the frequency that each animal's values deviated outside clinically relevant thresholds using this final dataset. Thresholds were set at 100, 80 and 70 for systolic blood pressure, mean arterial pressure and diastolic blood pressure, respectively. Finally, we calculated the variance for each outcome (for example, systolic blood pressure), for each animal across the entire dataset.

Formal weekly haemodynamic assessments. First, resting beat-by-beat arterial pressure, heart rate, and sympathetic nerve activity were recorded for 10 min to calculate mean values. Next, animals were subjected to a negative-pressure stimulus using our custom LBNP chamber. After 5 min of baseline the chamber pressure was reduced to −10 mmHg for 1 min. We calculated the delta value for each outcome during the final 30 s of the chamber being on, compared to baseline, to best quantify the ability of each animal to recovery from the stimulus. Finally, we calculated a linear model between haemodynamic values and the exact chamber pressure.

Coeliac ganglia stimulation recordings. Haemodynamic outcomes were recorded during stimulation of the coeliac ganglia (see 'Rodent electrophysiology'). Across stepwise increases in stimulation amplitude (range 0–400 μV), delta values were calculated compared to baseline values. For visualization (Extended Data Fig. 3) delta values and stimulation amplitudes are scaled 0–100% for each animal ($n = 4$).

Spinal cord segment mapping of haemodynamic responses. Systolic, diastolic and mean arterial pressure were derived on a beat-by-beat basis over 10 min to establish resting haemodynamics. The maximal haemodynamic response at each segment was extracted by taking 30 s of baseline before stimulation at that segment, and then the maximal blood pressure immediately before visible motor threshold. Therefore, one value (delta) was taken for: systolic blood pressure, diastolic blood pressure, mean arterial pressure, and heart rate for each segment, for each rat. Concordance between these values and sympathetic neuron densities (see 'Anatomical segmental density distributions') were then calculated using standard linear models. For non-human primates, $n = 3$ were used for functional mapping.

EES before and after successive dorsal rhizotomies. After establishing baseline haemodynamics EES was applied to induce a pressor response ($n = 5$). Delta values for each haemodynamic parameter (that is, systolic blood pressure, diastolic blood pressure, and mean arterial pressure) were then derived. Next, successive bilateral dorsal rhizotomies (see 'Dorsal rhizotomy' in 'Surgical procedures and post-surgical care') were completed beginning at T11 and finishing with T12. Between each rhizotomy EES was applied and delta values for each haemodynamic parameter calculated.

Optogenetic silencing. After establishing baseline haemodynamics, EES was initiated and the peak haemodynamic value taken. After 10 s of EES, a laser was initiated for 30 s. The minimum value during this time period was then calculated. Finally, a blunting ratio was calculated as the ratio of the decrease between the peak EES values and minimum value during the silencing during experimental (laser ON) trials compared to control trials (Extended Data Fig. 5).

Splanchnic axotomies. After establishing baseline haemodynamics EES was initiated and the peak delta values calculated for each parameter. Next, a splanchnic axotomy was performed (see 'Splanchnic ganglia manipulations' in 'Surgical procedures and post-surgical care'). The same calculation procedures were then completed following axotomy (Extended Data Fig. 5).

α_1 receptor blockade. After establishing baseline haemodynamics, EES was initiated and the peak delta values calculated for each parameter. After infusion of prazosin (10 μg kg^{-1}), EES was triggered every minute for 10 min and delta values were calculated. The minimum response value was taken during this time. A washout value was calculated after 30 min, which we found was sufficient time for the response to be re-instated (Extended Data Fig. 5).

Establishing natural system dynamics. The relationships between systolic blood pressure, rostral ventrolateral medulla firing rate, and sympathetic nerve activity, recorded at the sympathetic renal nerve, were assessed using a feed-forward neural network. A basic regression model was implemented using the 'keras' framework within R. We used a sequential model with two densely connected hidden layers, and an output layer that returns a single, continuous value. We then aimed to predict a given output (for example, sympathetic nerve activity) from a given input (for example, rostral ventrolateral medulla firing rate). We used an 20/80 test-train split, with each trial from each animal representing a discrete item. We evaluated the performance of the model for the uninjured and SCI groups separately using the significance of the correlation between the real and predicted output traces.

Wavelet decomposition. To assess the periodic content of a given time-series, wavelet decomposition was implemented using the 'WaveletComp' R package. We analysed the univariate frequency structure using the function 'analyze.wavelet' function with default parameters.

Single versus multiple haemodynamic hotspot stimulation. After establishing baseline haemodynamics, we assessed whether stimulating one hotspot (T12) was more or less efficacious than stimulating the three key identified haemodynamic hotspots. The order of the stimulations was randomized, to avoid bias towards either single or joint stimulation. We assessed the maximum change in haemodynamics in response to the stimulation for each of the conditions. For non-human primates, $n = 3$ were used.

Closed-loop control of haemodynamics. The efficacy of closed loop protocols was established through key primary outcome measures. These included: (1) target error, defined as the difference between the 'target' (baseline) haemodynamic value and the actual value during an orthostatic stimulus; (2) time outside target, defined as the amount of time (s) spent outside a given target threshold (for example, baseline blood pressure −10 mmHg), which were tuned according to the desired accuracy in a given situation; (3) the model coefficient of the linear relationship between the change in haemodynamics (for example, systolic blood pressure) and the pressure inside the negative-pressure chamber; (4) convergence, defined as the time until stabilization of haemodynamics (set conservatively at ±2 mmHg); and (5) the time to max amplitude, in the case of the brainstem-spinal cord versus biomimetic control comparisons. For non-human primates, $n = 2$ were used.

Neuromorphological analyses

Anterograde axon and synapse quantification from the RVLM. Axon density (mGFP) was measured using 3 confocal image stacks per region (above: T1 spinal cord, below: L1 spinal cord) per animal ($n = 4$ rats). Images were acquired with standard imaging settings and analysed using custom-written Fiji scripts according to previously described

methods. Confocal output images were binarized by means of an intensity threshold and divided into square regions of interest (ROI). The investigator was blinded during intensity thresholding. Synapse density was quantified on each segmented sympathetic ($ChAT^{ON}$) neurons using the area of each neuron and the area of colocalization, as defined using Squassh within ImageJ[58].

Evaluation of spinal cord contusion. The extent and location of spinal cord damage was evaluated in each experimental animal[48]. The lesion cavity was cut in serial horizontal sections (40 μm) that were stained using GFAP. For each lesion, we calculated the spared spinal cord surface with respect to the distance from the epicentre of the lesion, the spared area at the epicentre, and the total volume of damaged spinal cord tissue. The percentage of spared tissue at the epicentre was calculated using Fiji and normalized using the mean surface of sections rostral and caudal to the contusion, taking into account the compression of the spinal cord.

Anatomical segmental density distributions. To determine the segmental density of sympathetic pre-ganglionic neurons, neurons co-labelled with Fluorogold and NeuN were tabulated using ImageJ (Fiji, v.1.0), in four key autonomic nuclei (intermediolateral nucleus, central autonomic nucleus, lateral funiculus, and the intercalated nucleus) every 200 mm within each segment from T6 to L1 (Extended Data Fig. 3). Neurons from the left and right side were summed. Concordance between these counts and the response to electrical stimulation were examined by transforming the values into a 0–1 range for each segment and plotting them against the electrical stimulation.

Assessment of immediate early gene expression in splanchnic ganglia. To investigate the recruitment of the coeliac ganglia by our stimulation protocol, immunohistological staining for cells activity markers were performed on two groups of Lewis rats (Extended Data Fig. 5). For the first group ($n = 5$) animals were anaesthetized with urethane and stimulated for 30 min at T12. Our second group ($n = 5$) was a control, animals were anaesthetized with urethane for an hour, then overdosed with urethane. Stained sections were analysed using confocal microscopy (Zeiss LSM 800 with airyscan) resulting in high-resolution multi-channel images, with 15–20 identifiable cells on each. We then built a custom analysis pipeline able to automatically segment, localize, and quantify cell colocalization across the three key phenotypic parameters (NISSL + TH, NISSL + FOS, and TH + FOS). In brief, we implemented preprocessing steps using Fiji, as we have described[48]. Next, we leveraged a recently published pipeline for automated segmentation and colocalization[58]. For each channel, the optimal set of parameters were identified and used for all downstream analyses. All data were summarized and final quantifications completed using custom R scripts.

Dynamic registration and permutation test to determine spatial enrichment of histological signals. To determine spatial enrichment of axon density in the lateral horn of the spinal cord we implemented a custom image analysis pipeline that includes preprocessing, registration and combination of histological images from different rats. In brief, we implemented all preprocessing in Fiji, and all registration procedures in R, using the image analysis package 'imageR', and medical image registration package 'RNiftyReg'. After dynamic registration, we determined the spatial enrichment of histological signals using custom R scripts, based on a permutation procedure. We first define a region of interest and compute the intensity of fluorescence for this area. We then randomly generate one thousand permutations of our region of interest over the image, allowing us to compute the null distribution of the signal and test the region of interest against it. Empirical *P* values were then calculated.

Statistical procedures

All data are reported as mean values and individual data points. No statistical methods were used to predetermine sample sizes, but our sample sizes are similar to those reported in previous publications[48]. Haemodynamic assays were replicated three to five times, depending on the experiment, and averaged per animal. Statistics were then performed over the mean of animals. All statistical analysis was performed in R using the base package 'stats', with primary implementation through the 'tidyverse' and 'broom' packages. Tests used included one or two-tailed paired or independent samples Student's *t*-tests, one-way ANOVA for neuromorphological evaluations with more than two groups, and one- or two-way repeated-measures ANOVA for haemodynamic assessments, when data were distributed normally, tested using a Shapiro–Wilk test. Post hoc Tukey tests were applied when appropriate. For regressions, mixed model linear regression was used in cases of multiple observations, or else standard linear modelling. In cases where group size was equal to or less than three null hypothesis testing was not completed. The significance level was set as $P < 0.05$. Exclusions of data are noted in the relevant methods sections. Unless stated otherwise, experiments were not randomized, and the investigators were not blinded to allocation during experiments and outcome assessment.

Clinical implementation in humans

Patient description. The patient was a 38-year-old male who experienced a traumatic SCI at the C5 spinal segment treated with cervical fixation one year before enrollment in the study. The neurological status was evaluated according to the American Spinal Injury Association Impairment Scale (AIS)[59], and was classified as motor and sensory complete (AIS-A) (Extended Data Fig. 10a). Before enrolment, the patient was using 2.5 mg of midodrine hydrochloride 1–2 times per day as well as abdominal binders and compression garments daily to manage orthostatic hypotension.

Electrode array placement of electrical epidural stimulation implant. The patient underwent an array implantation of a three column (5-6-5), 16-contact paddle lead positioned below the T10 and T11 vertebral bodies and connected to a primary cell implantable pulse generator (IPG) (RestoreAdvanced SureScan neurostimulator, Medtronic) (Extended Data Fig. 10). The array was implanted over the T10-L1 spinal segments, which provides coverage over the haemodynamic hotspots identified in rats and non-human primates. The final positioning of the array was confirmed with computed tomography (CT; Revolution GSI, GE Healthcare) as well as T1- and T2-weighted imaging acquired using a1.5-T MRI Optima MR450w Scanner (Optima, GE Healthcare). These acquisitions allowed for the visualization of the spine, spinal cord, and site of injury (Extended Data Fig. 10), and verification of the final medio-lateral and rostro-caudal positions of electrode array, relative to spinal column. Clinical testing was approved by the University of Calgary Research Ethics Board (REB18-1592, REB19-0349).

Orthostatic challenge using a clinical tilt test. All test procedures were performed at least one month after surgical implantation of the electrode array. Before test days, the patient was informed to abstain from vigorous exercise for 24 h before testing, as well as to have abstained from caffeine, alcohol, cannabis, and withhold medications 12 h before testing. The patient was also informed to only consume a light breakfast the day of testing. Upon arrival during testing days, the patient was transferred to a table capable of head-up tilt (model 1211, MPI) with feet positioned on a footrest in an abducted position (Extended Data Fig. 10). We applied restraint straps to secure the patient below the knees and across the thighs, with the feet stabilized. The upper body was secured by two restraint straps that went from the hip region across to the contralateral shoulder. Resting supine blood pressure were recorded continuously for approximately 5 min to establish baseline values. We then tilted the patient upright up to a maximum of 70° while recording haemodynamic values and symptoms of orthostatic tolerance. Time to reach desired tilt angle from supine was achieved in less than 5 s.

Haemodynamic monitoring. Beat-to-beat blood pressure and heart rate was obtained via finger plethysmography (Finometer, Finapres Medical Systems) and collected using an analogue to digital converter (PowerLab, AD Instruments) at a sampling rate of 1,000 Hz (LabChart, AD Instruments). Beat-by-beat blood pressure was calibrated to brachial artery blood pressure collected using an arm cuff embedded and synchronized with the Finometer[60–64]. Heart rate, systolic pressure and diastolic pressures were recorded continuously throughout testing.

Symptoms of orthostatic intolerance. The patient was asked approximately every 1–3 min about their symptoms of orthostatic intolerance. The patient was asked to rank their symptoms between 1 and 10, with 1 being no symptoms at all, and 10 being feelings of dizziness, lightheadedness[17] or nausea[17,25]. The patient was instructed to notify the research team if they needed to be returned to the supine position.

Blood draws and circulating noradrenaline. Two 6-ml blood samples were obtained from the median cubital vein using a sterile 21 gauge straight needle during stimulator-off and stimulator-on conditions. To avoid false positives, the patient was asked to abstain from any beta-blocker, dihydropyridine calcium channel blocker, phenoxybenzamine, anxiolytics, or decongestants medications. Blood draws occurred after approximately 30 min resting in the supine position. Samples were collected in mauve top CATP tube (special catecholamine collection tube K2 EDTA with sodium metabisulphite). To ensure sample quality, before and immediately after, collection tubes were kept cold via immersion in crushed ice and kept in foil to reduce exposure to light. Samples were centrifuged for 10 min at 4 °C ± 2 °C and a speed of 1,200 relative centrifugal force (RCF). A minimum of 2 ml extracted plasma from each tube ($n = 2$ per condition) was analysed for catecholamines (noradrenaline, adrenaline, dopamine) by Calgary Lab Services using high-performance liquid chromatography electro-chemical detection (HPLC-ECD).

Sympathetic nerve activity recordings. Microneurography was used to acquire efferent postganglionic MSNA from the right common peroneal (fibular) nerve[65,66]. Palpation was used to locate the position of the common fibular nerve, followed by percutaneous insertion of a 2-MΩ tungsten microelectrode (FHC) into the nerve approximately 2 cm adjacent to a subcutaneous low impedance reference electrode. The MSNA signal was amplified (75,000×) and band-pass filtered (0.7–2.0 kHz) to obtain the raw neurogram (that is, muscle sympathetic spike activity) and then rectified and integrated (0.1-s time constant) to obtain a multi-unit (mean voltage) neurogram (Nerve Traffic Analyzer, Model 662C-4; University of Iowa). Owing to the impaired supraspinal influence on lower limb MSNA in this patient, there was a lack of spontaneous multi-unit MSNA bursts at rest and visually undetectable changes in neural activity during end expiratory apneas[67]. Thus, the recording microelectrode was confirmed to be near nerve fibres directed towards skeletal muscle by auditory feedback during tapping/palpation of the tibialis anterior/peroneal muscles and absent auditory feedback from light stroking of skin on the dorsal foot/lower shank (indicative of fibres directed towards the skin). These criteria have been shown previously to be indicative of microelectrode proximity to efferent post-ganglionic muscle sympathetic nerves[68]. All continuous data were digitized and stored using LabChart (version 8; PowerLab; AD Instruments) at a sampling frequency of 1,000 Hz except for the MSNA signal, which was sampled at 10 kHz.

After acquiring a stable recording site, a 3-min baseline commenced followed by progressive ramp stimulation of the epidural stimulator device. The stimulation was increased by 0.5 V every 30–60 s. Multi-unit MSNA data were analysed using a custom semi-automated LabView software program (National Instruments)[65]. Muscle sympathetic action potential spikes were identified as waveforms that matched a triphasic morphology with the main phase being negative[66]. The negative deflections were only assessed if they were <−0.45 V, as a threshold outside the baseline noise width across all stimulation conditions. In the case of spontaneous multi-unit bursts becoming visible in the multi-unit (mean voltage) neurogram during the stimulation, we would identify the bursts only if rising above three times the noise width. To investigate whether the multi-unit bursts were gated from a supraspinal influence arising from the arterial baroreceptors, we quantified the burst latency as the difference between preceding candidate ECG R spikes. Latencies had to fall within a 1.0 to 1.6 s range for the possibility for arterial baroreflex gating. We found that the mean burst latency was outside the normal range, at 0.774 s (0.597–0.982 s) on average.

Amplitude mapping and implementation of closed loop procedures. We found a linear relationship between stimulation amplitudes (that is, 0 to 7.5 mV; 120 Hz; 450 μs pulse width) and pressor responses (Extended Data Fig. 10). During the closed-loop implementation, we monitored the patient's haemodynamic parameters using the finger plethysmography device described previously (see 'Haemodynamic monitoring'). Baseline values were obtained in the supine position for approximately 5 min. The patient was tilted upright up to a maximum of 70 degrees to induce orthostatic challenge. Using a feature selection algorithm, we extracted the mean blood pressure throughout the procedure. From the extracted mean blood pressure, we programmed a continuous stimulation output based on: $-(\Delta\text{blood pressure}) \times \beta(-\Delta \times \beta)$, in which 'Δblood pressure' is the change in blood pressure from baseline to upright tilt, and 'β' is the proportional coefficient. Using clinically-approved devices stimulation intensity was scaled every 2 s based on the calculated stimulation output in real-time. We performed two cycles of stimulation on and stimulation off which lasted approximately 5 min for each condition during tilted upright position. We then quantified the target error values (see 'Closed loop control of haemodynamics') comparing the change in haemodynamics (that is, systolic blood pressure, mean arterial pressure and diastolic blood pressure) for both conditions. Stimulation was delivered using the N'VISION 8840 clinical controller.

Data analysis of spatial configurations. During an orthostatic challenge (see 'Orthostatic challenge using a clinical tilt test'), changes in blood pressure were recorded in response to different spatial electrode configurations. We tested two sets of multipolar configurations. The first set includes three multipolar configurations along the rostro-caudal axis (that is, rostral, middle and caudal spatial configurations), identified using a genetic algorithm, as we have previously described[12,21]. The second set is a comparison of the optimal rostro-caudal spatial configuration (that is, posterior root stimulation) versus when the electrodes are switched between anodes and cathodes (that is, posterior column stimulation). Blood pressure values were extracted from when the stimulation is off and during maximum stimulation amplitude for each spatial configuration (Extended Data Fig. 10). All blood pressure mean values and data points have been reported to compare stimulation off and stimulation on conditions for each spatial electrode configuration.

Questionnaires. The patient was asked three questions to compare experienced clinical burden before using EES and after using EES in their daily routine. The questions were as follows: (1) On a scale of 0 to 10, can you rate how orthostatic hypotension affected your quality of life?; (2) What dosage of midodrine do you take in a day (that is, milligrams per day)? and (3) How often do you use compression garments in a week (that is, days per week)?.

Reporting summary

Further information on research design is available in the Nature Research Reporting Summary linked to this paper.

Data availability

Data that support the findings and software routines developed for the data analysis will be made available upon reasonable request to the corresponding authors. Source data are provided with this paper.

45. Ramsey, J. B. G. et al. Care of rats with complete high-thoracic spinal cord injury. *J. Neurotrauma* **27**, 1709–1722 (2010).
46. Anderson, M. A. et al. Required growth facilitators propel axon regeneration across complete spinal cord injury. *Nature* **561**, 396–400 (2018).
47. Squair, J. W. et al. High thoracic contusion model for the investigation of cardiovascular function after spinal cord injury. *J. Neurotrauma* **34**, 671–684 (2016).
48. Asboth, L. et al. Cortico-reticulo-spinal circuit reorganization enables functional recovery after severe spinal cord contusion. *Nat. Neurosci.* **21**, 576–588 (2018).
49. Scheff, S. W., Rabchevsky, A. G., Fugaccia, I., Main, J. A. & Lumpp, J. E., Jr. Experimental modeling of spinal cord injury: characterization of a force-defined injury device. *J. Neurotrauma* **20**, 179–193 (2003).
50. van den Brand, R. et al. Restoring voluntary control of locomotion after paralyzing spinal cord injury. *Science* **336**, 1182–1185 (2012).
51. Krassioukov, A. V. & Weaver, L. C. Connections between the pontine reticular formation and rostral ventrolateral medulla. *Am. J. Physiol.* **265**, H1386–H1392 (1993).
52. Ueno, M., Ueno-Nakamura, Y., Niehaus, J., Popovich, P. G. & Yoshida, Y. Silencing spinal interneurons inhibits immune suppressive autonomic reflexes caused by spinal cord injury. *Nat. Neurosci.* **19**, 784–787 (2016).
53. Sundt, D., Gamper, N. & Jaffe, D. B. Spike propagation through the dorsal root ganglia in an unmyelinated sensory neuron: a modeling study. *J. Neurophysiol.* **114**, 3140–3153 (2015).
54. McIntyre, C. C. & Grill, W. M. Extracellular stimulation of central neurons: influence of stimulus waveform and frequency on neuronal output. *J. Neurophysiol.* **88**, 1592–1604 (2002).
55. Pan, C. et al. Shrinkage-mediated imaging of entire organs and organisms using uDISCO. *Nat. Methods* **13**, 859–867 (2016).
56. Lee, E. et al. ACT-PRESTO: Rapid and consistent tissue clearing and labeling method for 3-dimensional (3D) imaging. *Sci. Rep.* **6**, 18631 (2016).
57. Bria, A. & Iannello, G. TeraStitcher - a tool for fast automatic 3D-stitching of teravoxel-sized microscopy images. *BMC Bioinformatics* **13**, 316 (2012).
58. Rizk, A. et al. Segmentation and quantification of subcellular structures in fluorescence microscopy images using Squassh. *Nat. Protocols* **9**, 586–596 (2014).
59. Kirshblum, S. C. et al. International standards for neurological classification of spinal cord injury (revised 2011). *J. Spinal Cord Med.* **34**, 535–546 (2011).
60. Bogert, L. W. J. & van Lieshout, J. J. Non-invasive pulsatile arterial pressure and stroke volume changes from the human finger. *Exp. Physiol.* **90**, 437–446 (2005).
61. Jansen, J. R. et al. A comparison of cardiac output derived from the arterial pressure wave against thermodilution in cardiac surgery patients. *Br. J. Anaesth.* **87**, 212–222 (2001).
62. Westerhof, B. E., Gisolf, J., Stok, W. J., Wesseling, K. H. & Karemaker, J. M. Time-domain cross-correlation baroreflex sensitivity: performance on the EUROBAVAR data set. *J. Hypertens.* **22**, 1371–1380 (2004).
63. Wieling, W., Ganzeboom, K. S. & Saul, J. P. Reflex syncope in children and adolescents. *Heart* **90**, 1094–1100 (2004).
64. Whinnett, Z. I. et al. Multicenter randomized controlled crossover trial comparing haemodynamic optimization against echocardiographic optimization of av and VV delay of cardiac resynchronization therapy: the BRAVO trial. *JACC Cardiovasc. Imaging* **12**, 1407–1416 (2019).
65. Notay, K. et al. Validity and reliability of measuring resting muscle sympathetic nerve activity using short sampling durations in healthy humans. *J. Appl. Physiol.* **121**, 1065–1073 (2016).
66. Incognito, A. V. et al. Evidence for differential control of muscle sympathetic single units during mild sympathoexcitation in young, healthy humans. *Am. J. Physiol. Heart Circ. Physiol.* **316**, H13–H23 (2019).
67. Wallin, B. G. et al. Sympathetic single axonal discharge after spinal cord injury in humans: activity at rest and after bladder stimulation. *Spinal Cord* **52**, 434–438 (2014).
68. Incognito, A. V. et al. Pharmacological assessment of the arterial baroreflex in a young healthy obese male with extremely low baseline muscle sympathetic nerve activity. *Clin. Auton. Res.* **28**, 593–595 (2018).

Acknowledgements See Supplementary Notes. Support: Compute Canada, the Natural Sciences and Engineering Research Council, the Canadian Institutes of Health Research, Banting Fellowship, Alberta Innovates Health Solutions, Campus Alberta Neuroscience, the Libin Cardiovascular Institute, the Hotchkiss Brain Institute, PRAXIS, International Foundation for Research in Paraplegia, McCaig Institute for Bone and Joint Health, European Union's Horizon 2020 (no. 785907 Human Brain Project SGA2, no. 842578 and no. 665667), RESTORE: Eurostars E10889, OPTISTIM: Eurostars E!12743, the Swiss National Science Foundation (NCCR Robotics, 310030_185214, CRSII3_160696), European Research Council (ERC-2015-CoG HOW2WALKAGAIN 682999), and Bertarelli Foundation. M.A.A. is supported by a SNF Ambizione fellowship (PZ00P3_185728).

Author contributions J.W.S., M.G., L. Mahe, J.E.S., N.C., A.B., M.A.A., N.D.J., A.L., L. McCracken, I.J., C.M., J.G., Z.K.S., C.K., K.B., J.R., Q.B., E.M.M. and A.A.P. performed the rodent experiments and analysed the data. A.R. and M.C. performed computational experiments. J.B., G.C., E.B., Y.C. and Q.L. conducted the non-human primate experiments. J.W.S., R.D., S.K., C.M., F.B.W., R.B., N.B., E.M.M., T.D., G.S., X.K., N.V., F.F., S.P.L., G.C. and A.A.P designed hardware and software for neurostimulation. A.V.I., P.J.M., B.V., B.S., R.R., R.C., J.E.S., S.D., S.K.B., A.V.I., I.R. and A.A.P. performed the human experiments and analysed the data. G.C. and A.A.P. conceived and supervised the study. J.W.S., G.C. and A.A.P. wrote the paper, and all the authors contributed to its editing.

Competing interests G.C., J.B., J.W.S., A.A.P. and S.P.L hold various patents in relation with the present work. R.B. and N.B. are Medtronic employees. Y.C. and Q.L. are Motac neuroscience employees. E.B. is consultant and shareholder of Motac neuroscience. G.C., J.B., S.P.L. and A.A.P. are shareholders of Onward, a company with potential relationships with the invention.

Additional information

Supplementary information is available for this paper at https://doi.org/10.1038/s41586-020-03180-w.

Correspondence and requests for materials should be addressed to G.C. or A.A.P.

Peer review information *Nature* thanks Patrice Guyenet, Ryan Solinsky, Veronica Tom and the other, anonymous, reviewer(s) for their contribution to the peer review of this work.

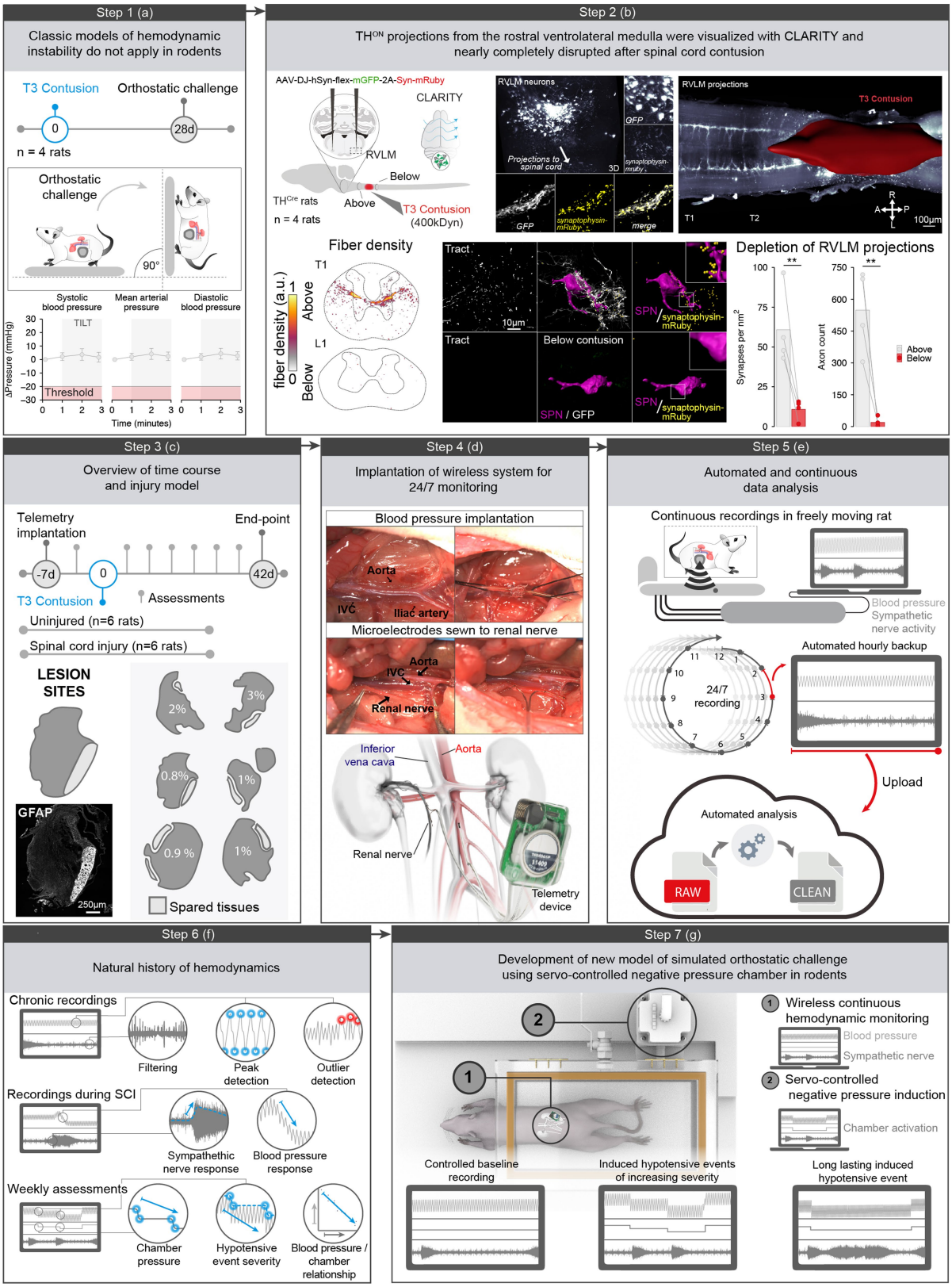

Extended Data Fig. 1 | See next page for caption.

Extended Data Fig. 1 | Development of a novel model of haemodynamic instability in rodents. Step 1 (a): We first tested the capacity for an orthostatic challenge to reduce blood pressure in rats 30 days after a T3 spinal cord injury ($n = 4$). Tilting rats 90° upright did not lead to any reduction in systolic blood pressure (one-way repeated measures ANOVA; $F_3 = 0.612$; $P = 0.62$), diastolic blood pressure (one-way repeated measures ANOVA; $F_3 = 1.105$; $P = 0.40$), or mean arterial pressure (one-way repeated measures ANOVA; $F_3 = 0.915$; $P = 0.47$). Data are mean ± s.e.m. Step 2(b): To confirm that our contusion model disrupted descending control of haemodynamics we used AAV-DJ-hSyn-flex-mGFP-2A-synaptophysin-mRuby injected into the RVLM of TH-Cre rats ($n = 4$) one month after T3 spinal cord injury. We found a near complete disruption of descending TH^{ON} sympatho-excitatory axons (paired one-tailed *t*-test; $t = 5.08$; $P = 0.007$) and synapses (paired one-tailed *t*-test; $t = 4.64$; $P = 0.009$) when comparing counts above and below the injury. Bar charts represent the mean with raw data overlaid. Step 3(c): Overview of the time-course used to examine the natural history of haemodynamic instability in uninjured ($n = 6$) and spinal cord injured animals ($n = 6$). Confirmation that the lesion site spared minimal white matter (identified using GFAP; mean = 2%). Step 4(d): We implanted a wireless recording system to monitor haemodynamics and sympathetic nerve activity. A blood pressure cannula was inserted into the abdominal aorta and microelectrodes sutured to the sympathetic renal nerve. Step 5(e): Data were recorded 24/7 and automatically uploaded to a server where automated analyses were triggered to quantify blood pressure and sympathetic nerve activity throughout the day and night. Step 6(f): We established the natural history of haemodynamic instability by recording the response to spinal cord injury and automatically detecting outliers (see Methods, 'Haemodynamic and sympathetic nerve activity monitoring') for blood pressure and sympathetic nerve activity data for a total of 7 weeks. Step 7(g): Because rats do not exhibit haemodynamic instability in response to an orthostatic challenge (see 'Step 1(a)'), we developed a servo-controlled negative-pressure approach whereby animals are placed in a chamber and the pressure is dropped and monitored in closed loop (see Methods, 'Implementation of a simulated orthostatic challenge in rodents and non-human primates'). $^*P < 0.05$; $^{**}P < 0.01$; $^{***}P < 0.001$.

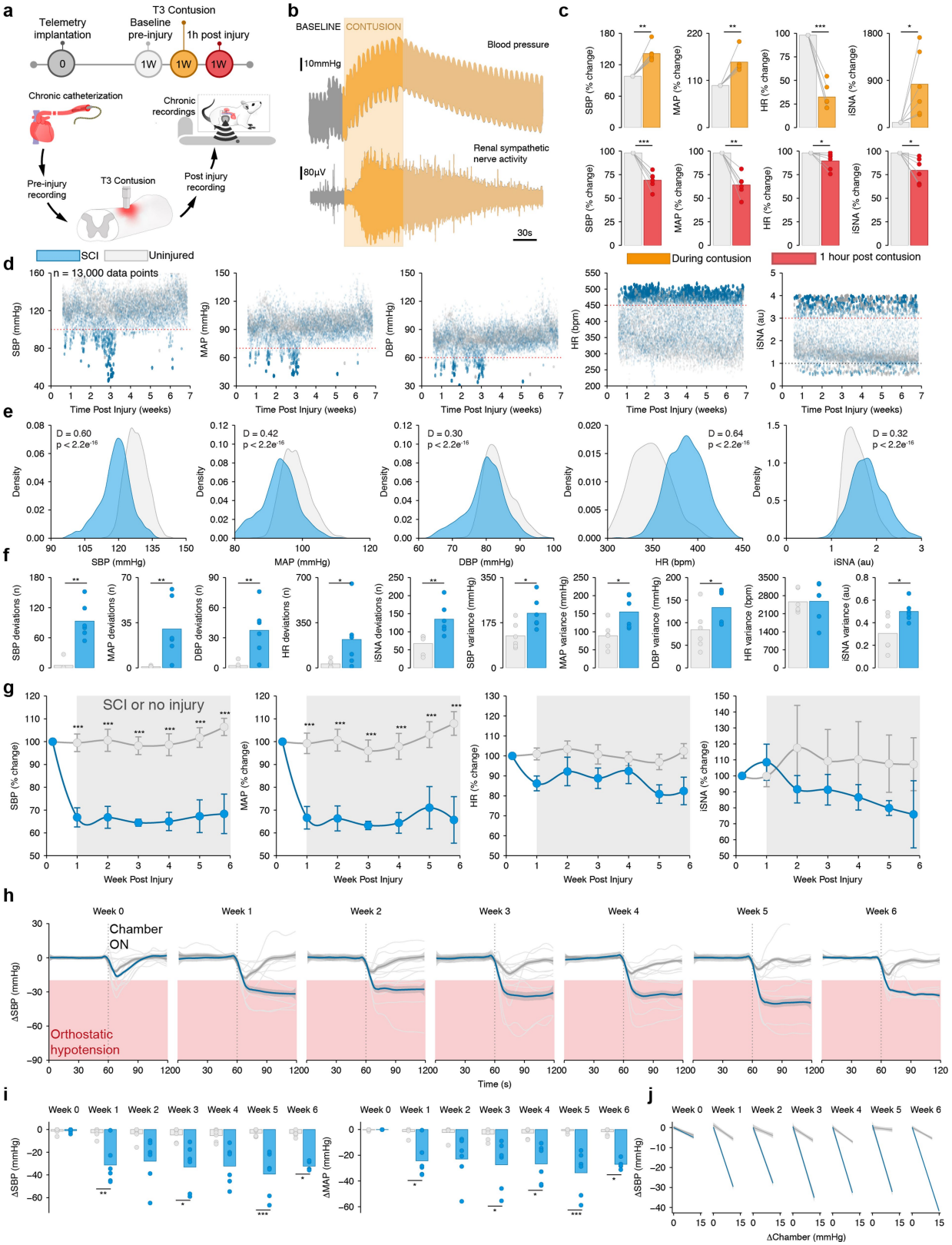

Extended Data Fig. 2 | See next page for caption.

Extended Data Fig. 2 | Rodent model develops haemodynamic instability across the natural history of spinal cord injury. a, We recorded haemodynamics and sympathetic nerve activity during and after the spinal cord contusion ($n = 6$). **b**, We observed an immediate increase in blood pressure and sympathetic nerve activity following the onset of the contusion. **c**, Quantifications revealed a significant increase in systolic blood pressure (paired one-tailed *t*-test; 91 mmHg vs 128 mmHg; $t = 5.40$; $P = 0.001$) and mean arterial pressure (paired one-tailed *t*-test; 63 mmHg vs 96 mmHg; $t = 4.50$; $P = 0.003$), a decrease in heart rate (paired one-tailed *t*-test; 309 bpm vs 100 bpm; $t = -10.26$; $P = 7.56 \times 10^{-5}$), and an increase in sympathetic nerve activity (paired one-tailed *t*-test; $t = 2.26$; $P = 0.037$) during contusion. These were followed by complete reversal after the contusion, where systolic blood pressure (paired one-tailed *t*-test; 116 mmHg vs 79 mmHg; $t = -5.97$; $P = 0.0009$), mean arterial pressure (paired one-tailed *t*-test; 85 mmHg vs 53 mmHg; $t = -5.14$; $P = 0.002$), sympathetic nerve activity (paired one-tailed *t*-test; $t = -3.29$; $P = 0.011$), and heart rate (paired one-tailed *t*-test; 350 bpm vs 313 bpm; $t = -2.91$; $P = 0.017$) decreased compared to pre-injury. **d**, We next established the natural history of haemodynamics using 24/7 recordings. We found that throughout the recording period animals with spinal cord injury deviated outside key thresholds representing 'normal' values (points scaled by size and transparency based on their deviation outside our set thresholds (dotted lines)). **e**, We found a left-shift in the distribution of haemodynamic values, and a right-ward shift in heart rate values, indicating generally lower blood pressure, higher heart rate, and more aberrant sympathetic nerve activity (Kolmogorov–Smirnov test; all $P < 2.2 \times 10^{-16}$). **f**, Quantifications revealed an increase in the number of deviations for systolic blood pressure (independent samples one-tailed *t*-test; $t = 5.92$; $P = 0.0005$), diastolic blood pressure (independent samples one-tailed *t*-test; $t = 3.68$; $P = 0.007$), mean arterial pressure (independent samples one-tailed *t*-test; $t = 3.23$; $P = 0.011$), heart rate (independent samples one-tailed *t*-test; $t = 2.0$; $P = 0.0499$), and sympathetic nerve activity (independent samples one-tailed *t*-test; $t = 3.20$; $P = 0.006$). We also found an increase in the variance of systolic blood pressure (independent samples one-tailed *t*-test; $t = 2.70$; $P = 0.011$), diastolic blood pressure (independent samples one-tailed *t*-test; $t = 2.01$; $P = 0.036$), mean arterial pressure (independent samples one-tailed *t*-test; $t = 2.85$; $P = 0.009$), and sympathetic nerve activity (independent samples one-tailed *t*-test; $t = 3.20$; $P = 0.006$), fitting the criteria for haemodynamic instability after SCI. **g**, Formal baseline recordings revealed that baseline systolic blood pressure (two-way repeated measures ANOVA; interaction effect $F_{6,1} = 7.05$; $P = 1.10 \times 10^{-5}$; all Tukey post hoc $P < 0.001$) and mean arterial pressure (two-way repeated measures ANOVA; interaction effect $F_{6,1} = 4.93$; $P = 0.0004$; all Tukey post hoc $P < 0.001$) were reduced, in agreement with spontaneous 24/7 data recordings. Data are mean ± s.e.m. **h**, We devised a closed-loop negative-pressure system to mimic an orthostatic challenge in rats. Animals with spinal cord injury could not respond to decreasing pressures, whereas uninjured animals responded and slowly recovered. This response was consistent across all six weeks post injury and is contrasted against week 0 (no injury for both groups). **i**, Quantification of this response revealed increased negative deltas for the spinal cord injury group for systolic blood pressure (two-way repeated measures ANOVA; interaction effect $F_{6,1} = 3.71$; $P = 0.003$; all Tukey post hoc $P < 0.05$) and mean arterial pressure (two-way repeated measures ANOVA; interaction effect $F_{6,1} = 4.20$; $P = 0.001$; all Tukey post hoc $P < 0.05$). **j**, After SCI we observed a time-dependent increase in the linear relationship between chamber pressure and blood pressure (likelihood ratio test of nested models; $P < 0.001$), indicating that haemodynamics cannot be stabilized during orthostatic challenge without a functioning baroreflex. In all panels, percentage change is presented for clarity as needed, while all statistics are calculated from raw values. Bar charts represent the mean with raw data overlaid. $^{*}P < 0.05$; $^{**}P < 0.01$; $^{***}P < 0.001$. HR, heart rate; iSNA, integrated sympathetic nerve activity; MAP, mean arterial pressure.

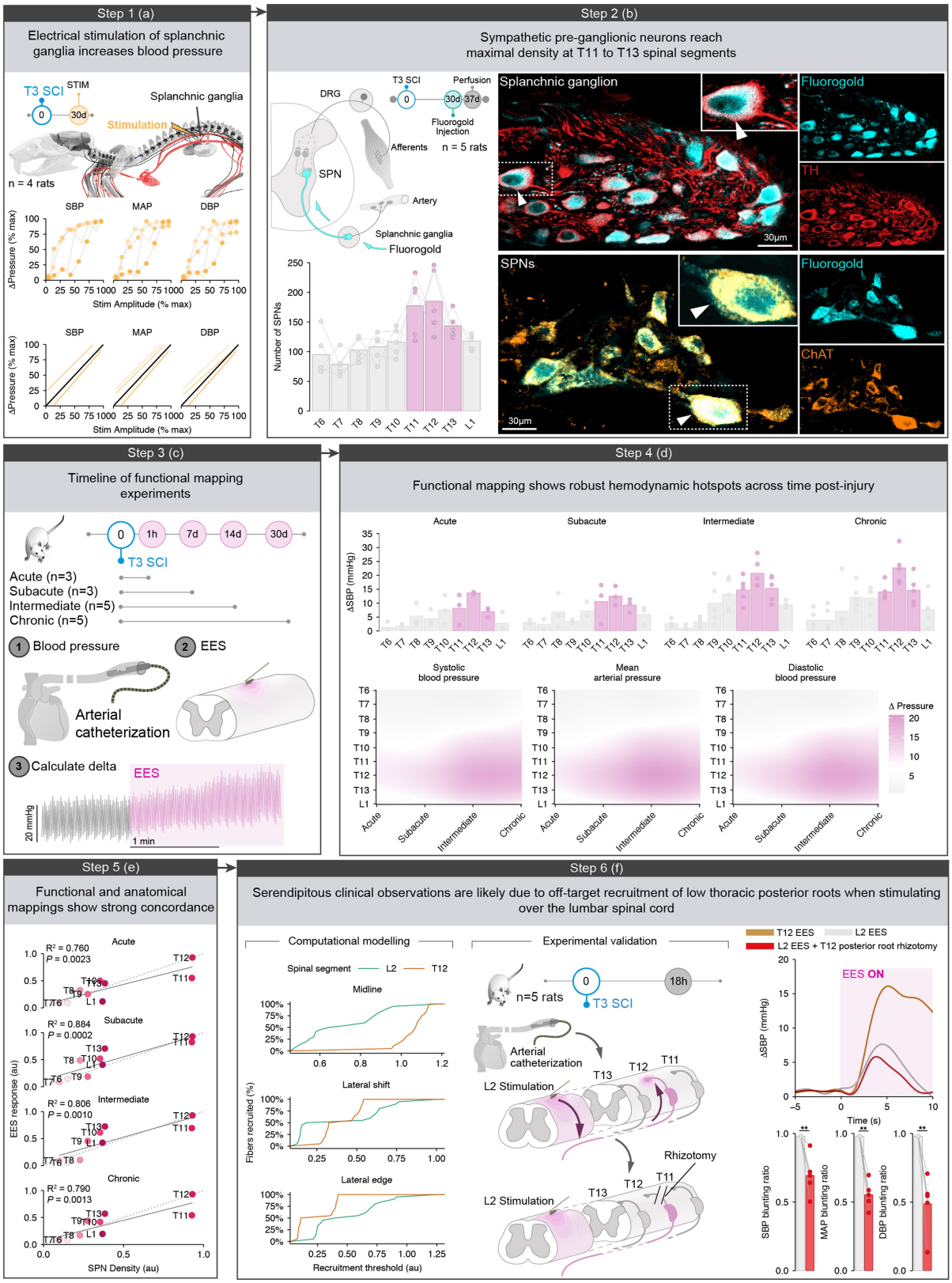

Extended Data Fig. 3 | See next page for caption.

Extended Data Fig. 3 | Functional and anatomical mapping reveal haemodynamic hotspots preferentially enriched to respond to epidural electrical stimulation. Step 1(a): We confirmed the role of the splanchnic ganglia in activating pressor responses. Electrical stimulation of splanchnic ganglia led to pressure responses that linearly increased with the stimulation amplitude ($n = 4$, linear mixed modelling; all $R^2 > 0.71$; all $P < 6.72 \times 10^{-12}$). These relationships were robust across systolic blood pressure, diastolic blood pressure, and mean arterial pressure. Step 2(b): Retrograde tracing of splanchnic ganglia using fluorogold labelled sympathetic pre-ganglionic neurons, which we confirmed using ChAT staining. Successful injection was confirmed in splanchnic ganglia by colocalization of fluorogold with TH. We found a peak density in the number of sympathetic pre-ganglionic neurons projecting to splanchnic ganglia in the lower thoracic segments. Step 3(c): We next completed functional mapping of the spinal cord by iterating through each segment and stimulating epidurally to activate pressor responses. We completed these experiments in animals one hour after injury (acute, $n = 3$), one-week after injury (sub-acute, $n = 3$), two weeks after injury (intermediate, $n = 5$), and four weeks after injury (chronic, $n = 5$). We recorded blood pressure using a terminal carotid catheterization preparation, and calculated the peak change in blood pressure during the stimulation. Step 4(d): We found that the response to targeted epidural electrical stimulation (EES) increased with time after injury, and that there was a haemodynamic hotspot in the lower thoracic spinal cord. Step 5(e): We found a linear relationship between the functional and anatomical mapping results, providing a clear rationale for the existence of the observed haemodynamic hotspot (linear modelling; all $R^2 > 0.72$; all $P < 0.003$). Step 6(f): We used computational modelling (Extended Data Fig. 4) and found that lateral edge (near root entrance/exit) placement of electrodes resulted in preferential recruitment of T12, even with EES placed at L2. This was in contrast to more midline stimulation where we saw preferential recruitment off L2. Indeed, with electrodes placed with a subtle 'lateral shift' the shift in recruitment to T12 already begins. We reasoned this may be the mechanism by which serendipitous clinical observations were made. We confirmed this hypothesis using a rhizotomy experiment, in which we cut the T12 root after stimulating with EES at L2 ($n = 5$). We found a significant blunting of the EES response in systolic blood pressure (paired one-tailed t-test; 10 mmHg vs 6.9 mmHg; $t = -3.95$; $P = 0.008$), mean arterial pressure (paired one-tailed t-test; 9.9 mmHg; vs 5.6 mmHg; $t = -6.03$; $P = 0.002$), and diastolic blood pressure (paired one-tailed t-test; 9.8 mmHg; vs 5.3 mmHg; $t = -5.90$; $P = 0.002$). Bar charts represent the mean with raw data overlaid.

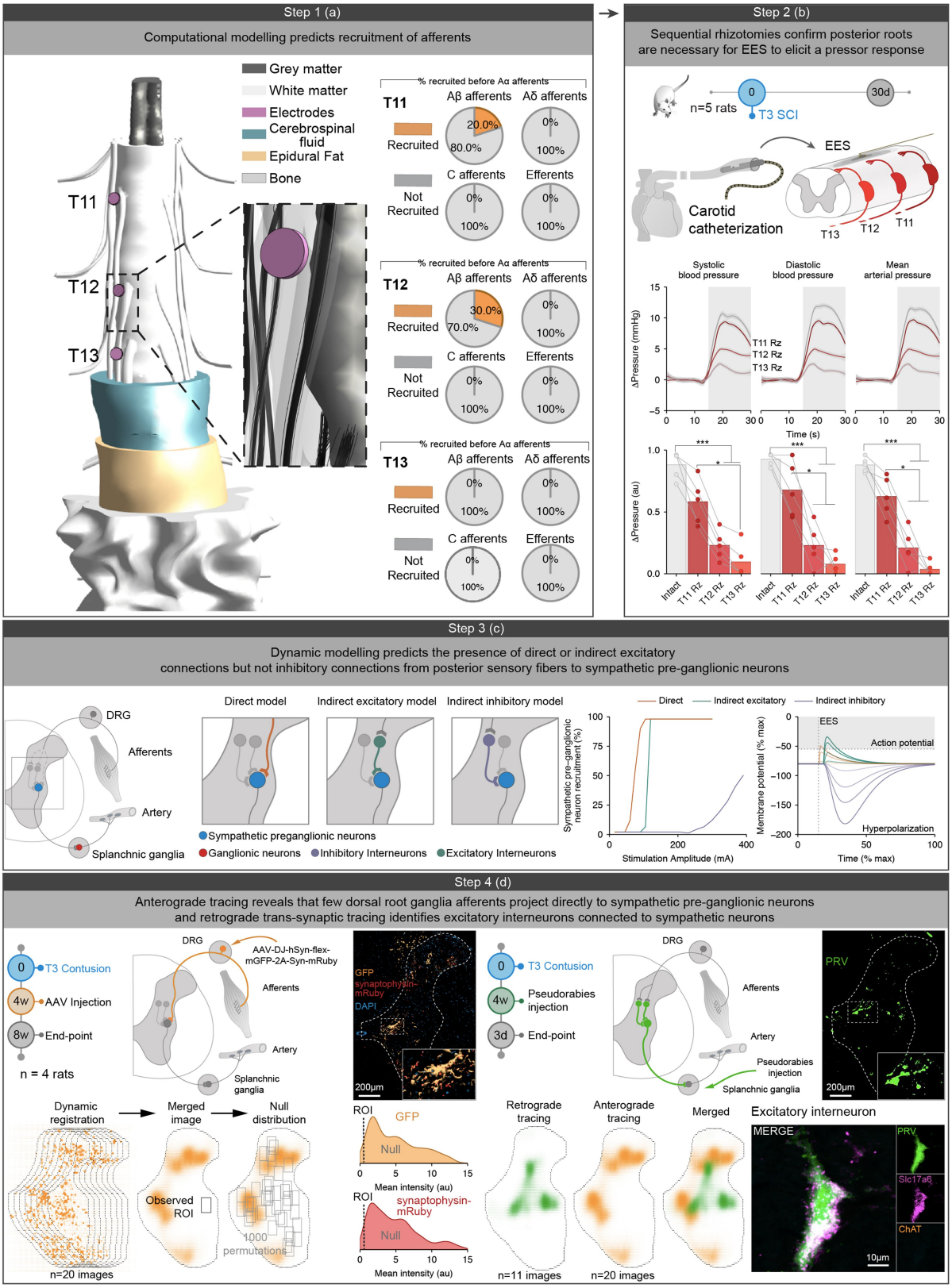

Extended Data Fig. 4 | See next page for caption.

Extended Data Fig. 4 | Epidural electrical stimulation induces pressor responses through the recruitment of posterior afferents and excitatory interneurons. Step 1(a): We developed a hybrid computational model based on real anatomical structures generated through high-resolution computed tomography and MRI scans. This model combines a geometrically realistic 3D finite element model of the spinal cord with realistic compartmental cable models of all afferent neurons, efferent neurons and some interneurons. We established a computational pipeline to obtain anisotropic tissue property maps, discretize the model, perform simulations using an electro-quasi-static solver and couple these simulations with NEURON-based electrophysiology models (Sim4Life by ZMT, www.zurichmedtech.com). We investigated the recruitment patterns of various afferent and efferent fibres within the spinal cord structure. We found that stimulation over the dorsal aspect of the spinal cord led to high levels of recruitment of major afferents, before any recruitment of efferent neurons directly from the stimulation. This suggested that epidural electrical stimulation activates pressor responses by recruiting afferents. Step 2(b): Next, we experimentally tested the hypothesis that pressor responses induced by EES were dependent on afferent activation. We completed successive dorsal rhizotomies at T11, T12 and T13 and found a graded reduction in the response to stimulation (one-way ANOVA; all $P < 0.001$; post hoc results indicated), with the largest decrease when removing T12, consistent with our functional and anatomical mapping results. Grey box indicates stimulation. Bar charts represent the mean with raw data overlaid. Step 3(c): Next, we developed a NEURON-based spiking neural network model composed of integrate-and-fire neurons to predict the presence of direct, indirect excitatory, and indirect inhibitory connections. Indirect inhibitory connections resulted in poor sympathetic pre-ganglionic neuron recruitment (left) and in the minimization of membrane potentials in response to increasing stimulation amplitude (right; various stimulation amplitudes indicated by alpha; action potential threshold indicated by horizontal dotted line; stimulation onset indicated by vertical dotted line). This suggested that pressor responses to EES likely are mediated by either direct, monosynaptic connections between afferents and sympathetic pre-ganglionic neurons or by indirect circuits including excitatory interneurons. Step 4(d): We completed anterograde tracing of the dorsal root ganglia. Using dynamic image registration we generated a digital dorsal horn whereby we could select a region of interest (ROI; grey box) and determine the mean intensity ('Observed ROI') of either axons (orange) or synapses (red). Using 1000 bootstraps of random ROIs as a null distribution we found a depletion of axons (empirical $P = 0.019$) and synapses (empirical $P = 0.001$) in the intermediolateral column. We confirmed this result by counting neurons with appositional synapses on $ChAT^{ON}$ neurons in the ventral horn versus the lateral horn and found a similar statistical depletion ($n = 10$ images, 294 neurons; Fisher's exact test; odds ratio (OR): 0.082; $P < 2.2 \times 10^{-16}$). This suggested that the most likely circuit mediating these responses instead included an excitatory interneuron. We therefore completed retrograde trans-synaptic tracing and found interneurons trans-synaptically connected to splanchnic ganglia that were SLC17A6 positive, and had VGLUT1 synaptic puncta in their immediate vicinity (see Fig. 2), suggesting direct connections with large diameter afferents. $^{*}P < 0.05$; $^{**}P < 0.01$; $^{***}P < 0.001$. Rz, rhizotomy.

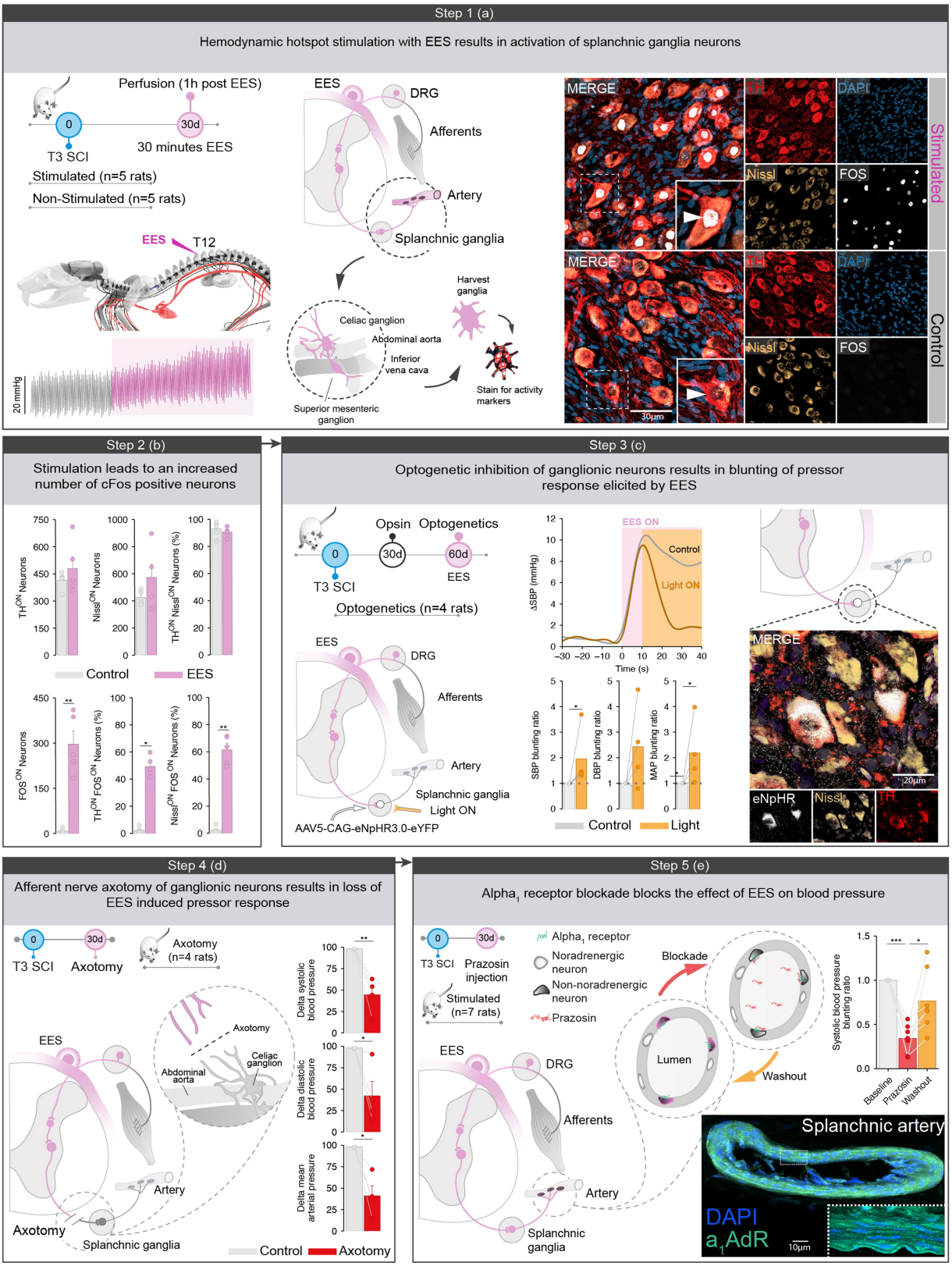

Extended Data Fig. 5 | See next page for caption.

Extended Data Fig. 5 | Epidural electrical stimulation induces pressor responses through the recruitment of splanchnic ganglia. Step 1(a): To determine whether epidural electrical stimulation activated splanchnic ganglia we stimulated rats with T3 spinal cord injury for 30 min ($n = 5$), or did not stimulate them ($n = 5$). We collected the splanchnic ganglia and subjected them to immunohistochemisty. We stained each section for TH, FOS (immediate early gene), DAPI, and NISSL to confirm neuronal phenotypes. We then used an automatic cell segmentation algorithm to identify cells that coexpressed TH, NISSL and/or FOS. Step 2(b): Quantifications revealed that animals stimulated with 30 min of EES had more FOS-positive neurons than unstimulated rats (independent samples one-tailed *t*-test; $t = 6.56$; $P = 0.001$), and that these neurons colocalized with TH and NISSL stains (both $P < 0.001$). Step 3(c): We next completed two loss of function studies to examine the causal role of the splanchnic ganglia in the pressor responses to EES. We conducted an optogenetics silencing experiment ($n = 4$) and an axotomy experiment whereby we surgically severed the connection between the sympathetic pre-ganglionic neurons in the spinal cord and the splanchnic ganglia ($n = 4$). We completed these experiments on animals 60 days after T3 spinal cord injury. For optogenetics experiments viral injections occurred at 30 days after injury. Activating the inhibitory opsin eNpHr3.0 with yellow light suppressed the pressor response to EES, and therefore increased the difference between the peak response to EES and the minimum response during light (or control) for systolic blood pressure (independent samples one-tailed *t*-test; 7 mmHg vs 12 mmHg; $t = 2.90$; $P = 0.031$) and mean arterial pressure (independent samples one-tailed *t*-test; 7 mmHg vs 13 mmHg; $t = 2.60$; $P = 0.040$). Step 4(d): Axotomy of the connection between sympathetic pre-ganglionic neurons and splanchnic ganglia likewise blunted the pressor response for systolic blood pressure ($n = 4$; independent samples one-tailed *t*-test; 20 mmHg vs 9.2 mmHg; $t = -4.54$; $P = 0.001$), diastolic blood pressure (independent samples one-tailed *t*-test; 19.6 mmHg vs 7 mmHg; $t = -2.40$; $P = 0.048$), and mean arterial pressure (independent samples one-tailed *t*-test; 19 mmHg vs 7 mmHg; $t = -3.08$; $P = 0.027$). These experiments indicate the splanchnic ganglia are necessary to induce a pressor response with EES. Step 5(e): We next tested whether blocking α_1 receptors on systemic blood vessels would blunt the response to EES. We administered prazosin intravenously and found an immediate loss of pressor responses to EES ($n = 7$). The response returned after drug washout (one-way repeated measures ANOVA; 18 mmHg vs 5.7 mmHg vs 13.1 mmHg; $F_2 = 15.63$; $P = 0.0001$; Tukey HSD). $^*P < 0.05$; $^{**}P < 0.01$; $^{***}P < 0.001$.

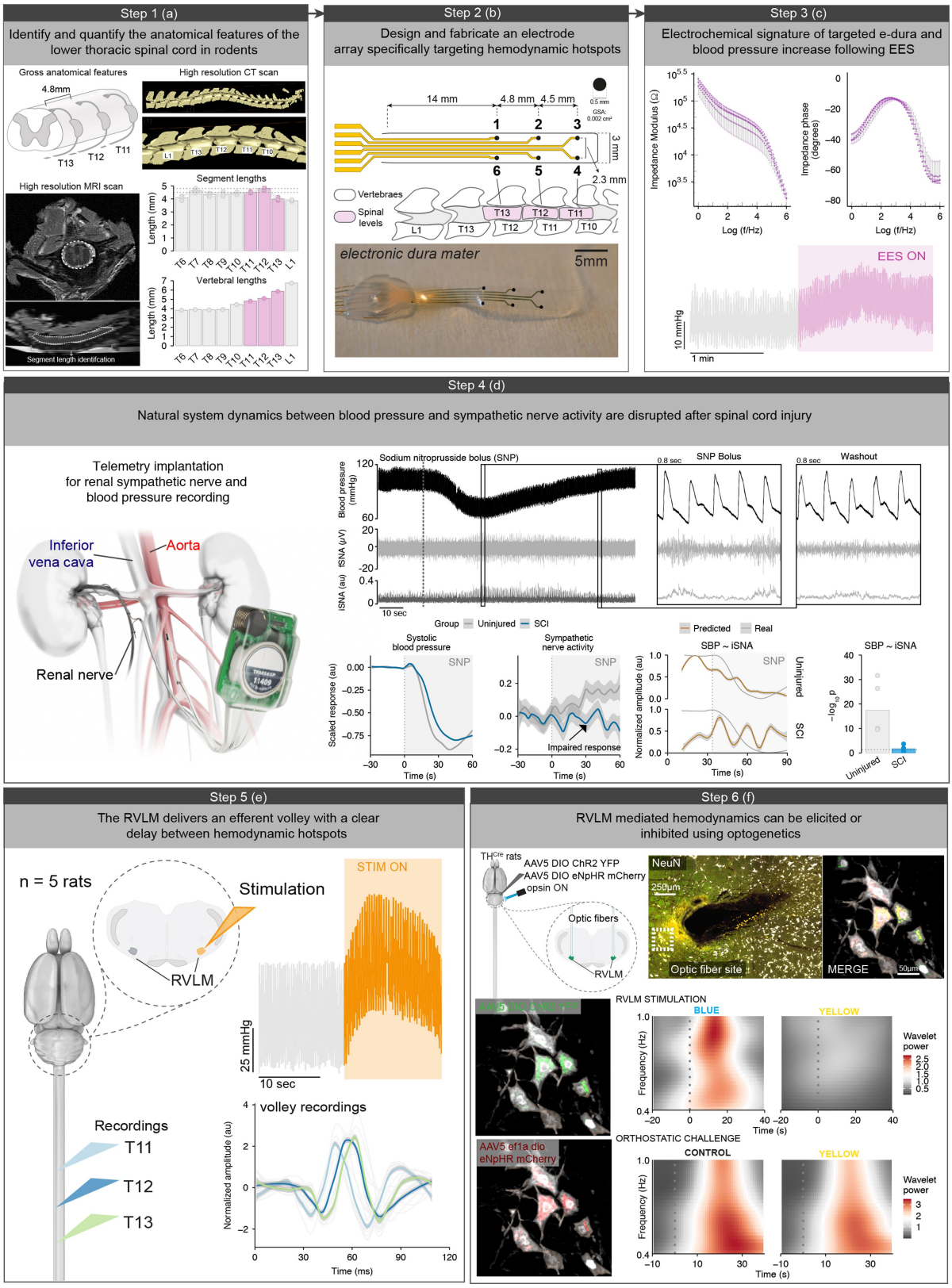

Extended Data Fig. 6 | See next page for caption.

Extended Data Fig. 6 | Mechanistic insight enabled the development of a targeted electronic dura mater and biomimetic stimulation strategy to recapitulate the natural dynamics of the sympathetic nervous system. Step 1(a): To develop the spatial features of an electrode array specifically targeting haemodynamic hotspots we first quantified all the features of the low thoracic spinal column. We measured the precise length of each spinal segment and vertebrae using a combination of gross anatomical dissections, high resolution computed tomography scans, and custom MRI sequences. Step 2(b): We used these anatomical features, driven by the identification of haemodynamic hotspots to develop an electronic dura mater specifically targeting T11, T12 and T13 spinal segments. Detailed dimensions of the active stimulation sites (500 µm diameter, 0.002 cm^2 geometric surface area). Step 3(c): When placed on the spinal cord, the array increases blood pressure and all electrodes are functional. Top, electrochemical impedance spectrum (modulus, left and phase, right) of an electrode array acquired in vitro post-fabrication. Step 4(d): To recapitulate the natural dynamics of the sympathetic nervous system we first recorded neural activity from the renal sympathetic nerve and blood pressure from the descending aorta. We measured these signals in response to a hypotensive stimulus (sodium nitroprusside (SNP)) in both injured and uninjured animals ($n = 5$; uninjured example shown). We found that there was an impaired response in the sympathetic nerve activity after SCI. To quantify the changes in these dynamics we trained a feed-forward neural network to predict a continuous output from a given input. For example, predicting systolic blood pressure from sympathetic nerve activity (iSNA). We found that in uninjured animals, there were strong correlations whereby the model could predict one from the other. In injured animals this correlation was absent. Here, we show the ability of the model to predict SBP from iSNA in response to this stimulus (strength of correlation (Pearson correlation) presented as $-\log_{10}(P)$ for each group). Responses are presented on a normalized delta scale to account for absolute differences between animals. Step 5(e): To understand the timing delay of RVLM activation to sympathetic outflow from the spinal cord we stimulated the RVLM electrically, and measured the efferent volley over T11, T12 and T13 ($n = 5$). Stimulation of the RVLM dramatically increased blood pressure, confirming localization of the stimulation. We then measured the delay between action potentials in response to 100 Hz 10 s pulse trains of RVLM stimulation and found a 2.5 ± 0.4 ms delay between segments. Representative traces across segments are shown for one animal. We therefore integrated this delay into the stimulation design between segments. Step 6 (f): Finally, to understand the precise role of frequency dynamics in blood pressure control we stimulated the RVLM using optogenetics in TH-Cre rats. We found that stimulation with blue light led to a robust increase in wavelet spectrogram within the 0.4–1.0 Hz band (paired samples one-tailed t-test; $t = 2.67$; $P = 0.028$). This was in contrast to activation of an inhibitory opsin using a yellow laser (which would, in this case, inhibit the RVLM due to the presence of an inhibitory opsin), which showed significantly less activation compared to blue light (paired samples one-tailed t-test; $t = 2.44$; $P = 0.035$). In response to an orthostatic challenge, the wavelet power response in uninjured rats was less pronounced in the presence of inhibitory (yellow) light (bottom; independent samples one-tailed t-test; $t = 4.04$; $P = 0.008$). $^*P < 0.05$; $^{**}P < 0.01$; $^{***}P < 0.001$.

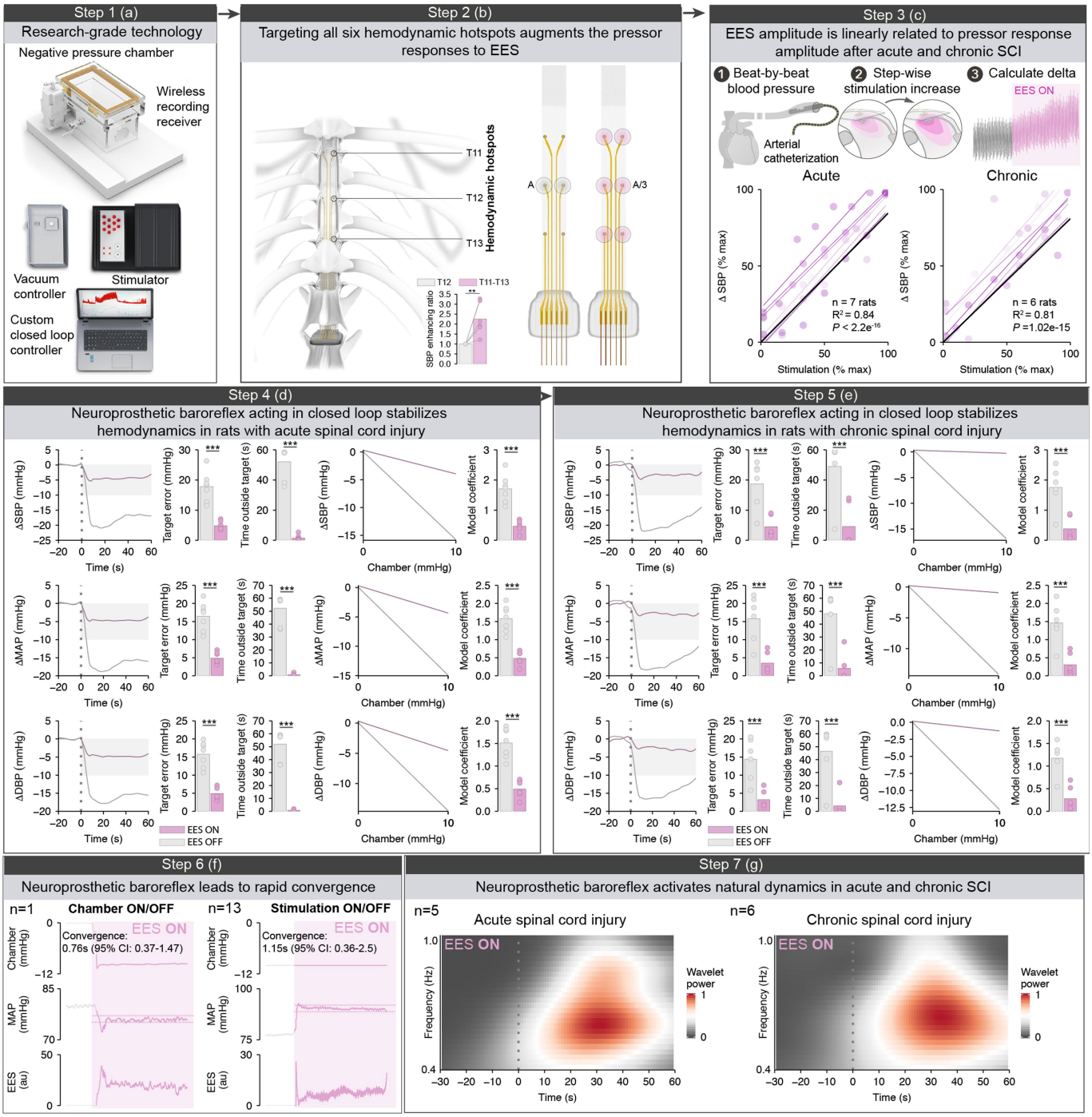

Extended Data Fig. 7 | See next page for caption.

Extended Data Fig. 7 | Neuroprosthetic baroreflex implemented in rodents with SCI. Step 1(a): We tested whether we could stabilize haemodynamics using the neuroprosthetic baroreflex, operating in a closed loop, in animals with acute ($n = 7$; 12 h after injury) and chronic ($n = 6$; one month after injury) T3 spinal cord injury. We implemented the neuroprosthetic baroreflex within research-grade technology to achieve precise control over stimulation parameters. Step 2(b): Schematic of electronic dura mater electrode arrays targeting haemodynamic hotspots. Bar chart shows relative pressor responses (systolic blood pressure; $n = 5$, independent samples one-tailed t-test; $t = 3.90$; $P = 0.006$). Step 3(c): We found a linear relationship between stimulation amplitude and the pressor response to stimulation in both animals with acute (mixed model linear regression; $R^2 = 0.84$, $P < 2.2 \times 10^{-16}$) and chronic (mixed model linear regression; $R^2 = 0.81$, $P < 1.0 \times 10^{-15}$) spinal cord injury. Step 4(d): We completed a series of trials to test the ability of the neuroprosthetic baroreflex to stabilize haemodynamics in rats with acute spinal cord injury. The neuroprosthetic baroreflex was activated in a closed loop before the activation of the lower-body negative-pressure chamber. In trials where the stimulation was ON, we found a reduction in the target (baseline) error (paired samples one-tailed t-test; systolic blood pressure (SBP): $t = -6.12$, $P = 5.50 \times 10^{-4}$; mean arterial pressure (MAP); $t = -6.08$, $P = 4.48 \times 10^{-4}$; diastolic blood pressure (DBP); $t = -5.85$, $P = 4.34 \times 10^{-4}$) reduced time outside key thresholds (–10 mmHg; paired samples one-tailed t-test; SBP: $t = -12.52$, $P = 9.94 \times 10^{-6}$; MAP; $t = -12.29$, $P = 8.83 \times 10^{-6}$; DBP; $t = -11.73$, $P = 1.15 \times 10^{-5}$), a restoration of the nonlinear relationship between blood pressure and chamber pressure, and a concomitant reduction in the linear model coefficient (likelihood ratio test of nested models; all $P < 0.001$). These quantifications held for systolic blood pressure (top), diastolic blood pressure (middle), and mean arterial pressure (bottom). Step 5(e): We completed the exact same experiments on animals with chronic spinal cord injury and found similar results to those of the acutely injured rats. Specifically, in trials where the stimulation was ON, we found a reduction in the target (baseline) error (paired samples one-tailed t-test; SBP: $t = -3.84$, $P = 0.006$; MAP; $t = -3.83$, $P = 0.006$; DBP; $t = -3.83$, $P = 0.006$), reduced time outside key thresholds (–10 mmHg; paired samples one-tailed t-test; SBP: $t = -4.37$, $P = 0.004$; MAP; $t = -4.43$, $P = 0.003$; DBP; $t = -4.21$, $P = 0.004$), a restoration of the nonlinear relationship between blood pressure and chamber pressure, and a concomitant reduction in the linear model coefficient (likelihood ratio test of nested models; all $P < 0.001$). These quantifications held for systolic blood pressure (top), diastolic blood pressure (middle), and mean arterial pressure (bottom). Step 6(f): We found that in response to stimulation blood pressure rapidly reached the set-point, with convergence times of 0.76 s in the example case presented in Fig. 3, and 1.15 s (95% confidence interval: 0.36–2.5 s) across $n = 13$ animals in response to the negative-pressure chamber. In this case convergence was defined as stable within 2.5 mmHg. Step 7(g): The neuroprosthetic baroreflex, acting in closed loop, re-established natural frequency dynamics (increased wavelet power in the 0.4–1.0 Hz spectrogram) in both animals with acute (paired samples one-tailed t-test; $t = 4.46$; $P = 0.002$) and chronic SCI (paired samples one-tailed t-test; $t = 3.37$; $P = 0.014$). $^*P < 0.05$; $^{**}P < 0.01$; $^{***}P < 0.001$.

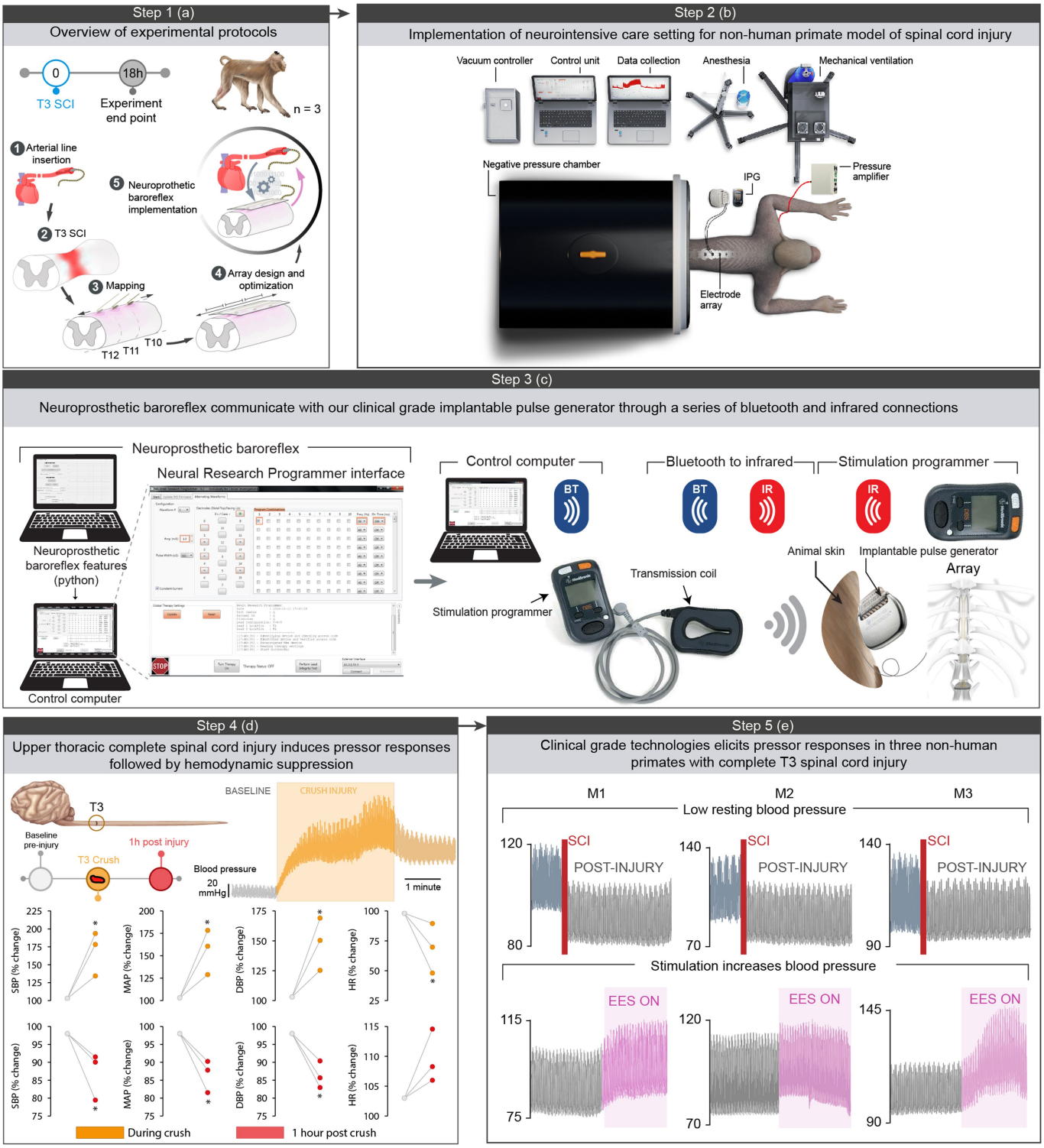

Extended Data Fig. 8 | See next page for caption.

Extended Data Fig. 8 | Translation of the neuroprosthetic baroreflex to non-human primates. Step 1(a): To further establish the efficacy of the neuroprosthetic baroreflex, we performed experiments in three non-human primates. First, we measured arterial blood pressure using an invasive catheter in the subclavian artery. Next, we performed a T3 spinal cord injury to mimic the experimental conditions of our rodent experiments. We next mapped the pressor responses to epidural stimulation from T7 to L3. We combined these results with ex vivo dissections of the anatomical dimensions of the lower thoracic spinal cord in rhesus macaques ($n = 3$) to design an electronic dura mater. Finally, we implemented all the features of the neuroprosthetic baroreflex. Step 2(b): We tested the efficacy of the neuroprosthetic baroreflex specifically within the context of acute traumatic SCI. We emulated all the features of standard neurointensive care including arterial blood pressure measurements, clinical grade anaesthesia (intravenous propofol), as well as temperature and respiration control. We integrated our stimulation approach into clinical-grade technologies using an implantable pulse generator and a spatially selective spinal implant. Step 3(c): All the features of the neuroprosthetic baroreflex were injected into our previously used clinical-grade stimulation approach. In brief, the neuroprosthetic baroreflex received beat-by-beat continuous blood pressure to provide closed loop control. Stimulation output control was sent to the neural research programmer interface, which communicates with the implantable pulse generator through a series of Bluetooth and infrared links. These commands were then sent directly to the customized spinal implant. Step 4(d): Similar to rodent experiments, we found that T3 spinal cord injury induced a significant surge in systolic blood pressure (paired one-tailed *t*-test; 127 mmHg vs 213 mmHg; $t = 4.15$; $P = 0.027$), mean arterial pressure (paired one-tailed *t*-test; 110 mmHg vs 172 mmHg; $t = 3.96$; $P = 0.029$), diastolic blood pressure (paired one-tailed *t*-test; 102 mmHg; vs 151 mmHg; $t = 3.80$; $P = 0.031$), and an accompanying decrease in heart rate (paired one-tailed *t*-test; 111 bpm vs 76 bpm; $t = -4.05$; $P = 0.028$). By one-hour after injury, we observed clinically relevant neurogenic shock, characterized by decreased systolic blood pressure (paired one-tailed *t*-test; 127 mmHg vs 110 mmHg; $t = -3.20$; $P = 0.043$), mean arterial pressure (paired one-tailed *t*-test; 110 mmHg vs 95 mmHg; $t = -5.23$; $P = 0.017$), and diastolic blood pressure (paired one-tailed *t*-test; 96 mmHg vs 102 mmHg; $t = -6.24$; $P = 0.012$). Step 5(e): Despite the fact that we observed an immediate decrease in resting blood pressure, epidural electrical stimulation was able to cause an immediate and transient pressor response in all three animals. In all cases, where percentage change is presented statistics were completed on raw values. $^{*}P < 0.05$; $^{**}P < 0.01$; $^{***}P < 0.001$.

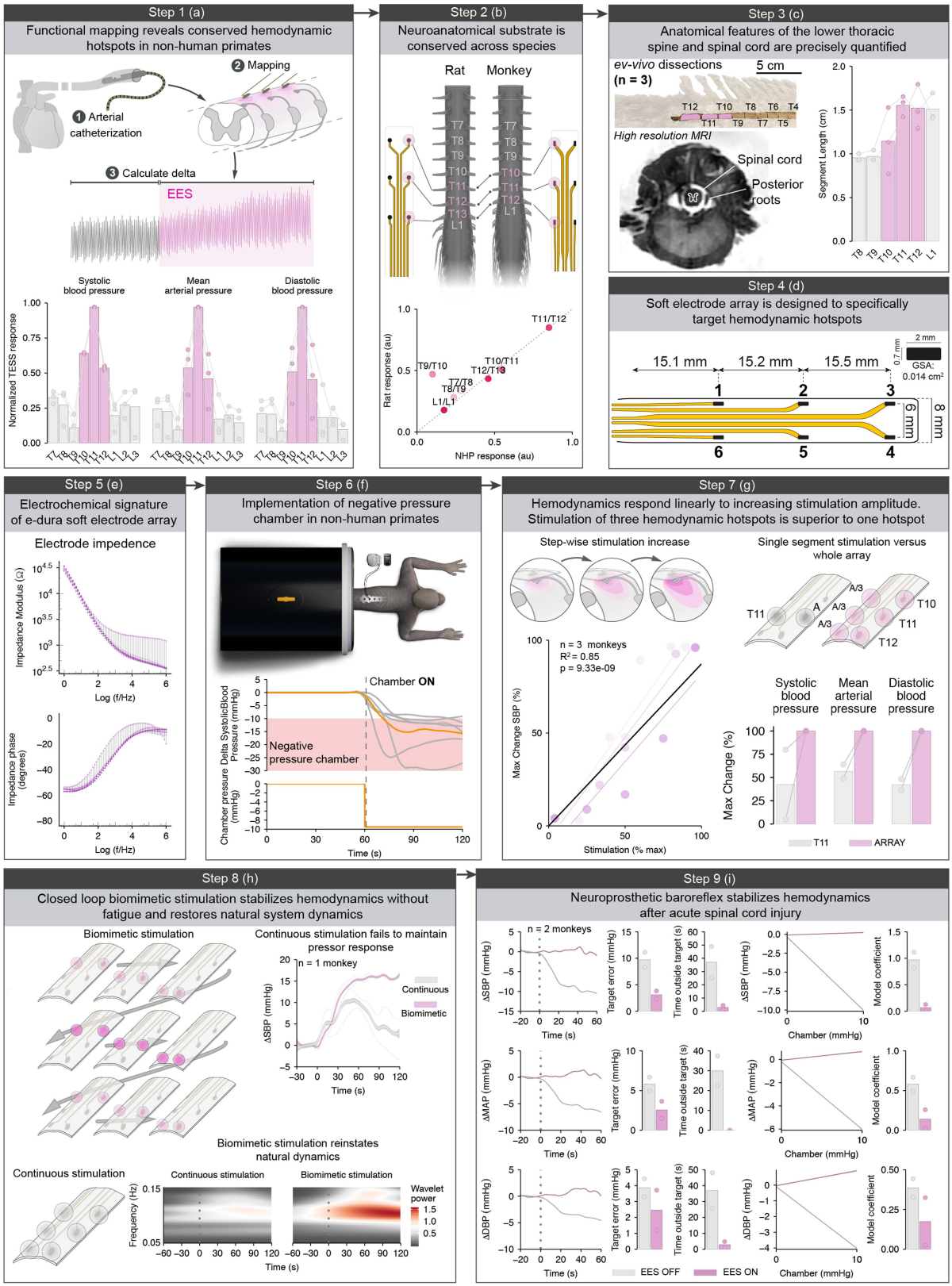

Extended Data Fig. 9 | See next page for caption.

Extended Data Fig. 9 | Neuroprosthetic baroreflex implemented in non-human primates with spinal cord injury. Step 1(a): We recorded blood pressure using an axillary artery catheterization preparation, and calculated the peak change in blood pressure during stimulation. We found that there was a haemodynamic hotspot in the lower thoracic spinal cord, specifically over segments T10, T11 and T12. Step 2(b): Accounting for the offset in segments between species, we found a linear relationship between the functional mapping results in rats and the functional mapping results in non-human primates, further confirming the localization of a haemodynamic hotspot in the last three thoracic segments (linear modelling; $R^2 = 0.65$; $P = 0.018$). Step 3(c): To develop the spatial features of an electrode array specifically targeting haemodynamic hotspots in the non-human primate we quantified all the features of the low thoracic spinal column. We measured the precise length of each spinal segment and vertebra using a combination of gross anatomical dissections, high resolution computed tomography scans, and custom MRI sequences. Step 4(d): We used these anatomical features, driven by the identification of haemodynamic hotspots to develop an electronic dura mater specifically targeting T10, T11 and T12 spinal segments. Detailed dimensions of the active stimulation sites (0.7 mm diameter, 0.014 cm^2 geometric surface area). Step 5(e): Electrochemical impedance spectrum (modulus, left and phase, right) of an electrode array acquired in vitro post-fabrication indicates functional, low-impedance electrodes. Step 6(f): We fully implemented a negative-pressure chamber designed to fit a non-human primate to induce a stimulated orthostatic challenge. We found that stimulation using the chamber led to an immediate and consistent decrease in blood pressure. Step 7(g): We next implemented our biomimetic stimulation protocols. We found a linear relationship between stimulation amplitude and the pressor response ($n = 3$ monkeys; linear modelling, $R^2 = 0.85$; $P = 9.33 \times 10^{-5}$). Compared to stimulating only one hotspot, stimulating with all three sets of electrodes, and therefore targeting each haemodynamic hotspot led to a more robust increase in blood pressure ($n = 2$ monkeys). Step 8(h): Implementation of the neuroprosthetic baroreflex, acting in closed loop, led to sustained increases in blood pressure that did not fatigue ($n = 1$ monkey). In comparison, continuous open-loop stimulation, using the same stimulation parameters, elicited an increase in blood pressure that was immediately followed by rapid fatigue. For continuous stimulation, the amplitude was set to the maximum observed stimulation value in the trials with the closed-loop controller. Only biomimetic stimulation re-established the natural frequency dynamics, revealed using wavelet decomposition ($n = 2$ monkeys). Step 9(i): Using this closed loop approach, we found a reduction in the target (baseline) error, reduced time outside key thresholds (−5 mmHg; −2 mmHg for diastolic blood pressure), a restoration of the nonlinear relationship between blood pressure and chamber pressure, and a concomitant reduction in the linear model coefficient. These quantifications held for systolic blood pressure (top), diastolic blood pressure (middle), and mean arterial pressure (bottom).

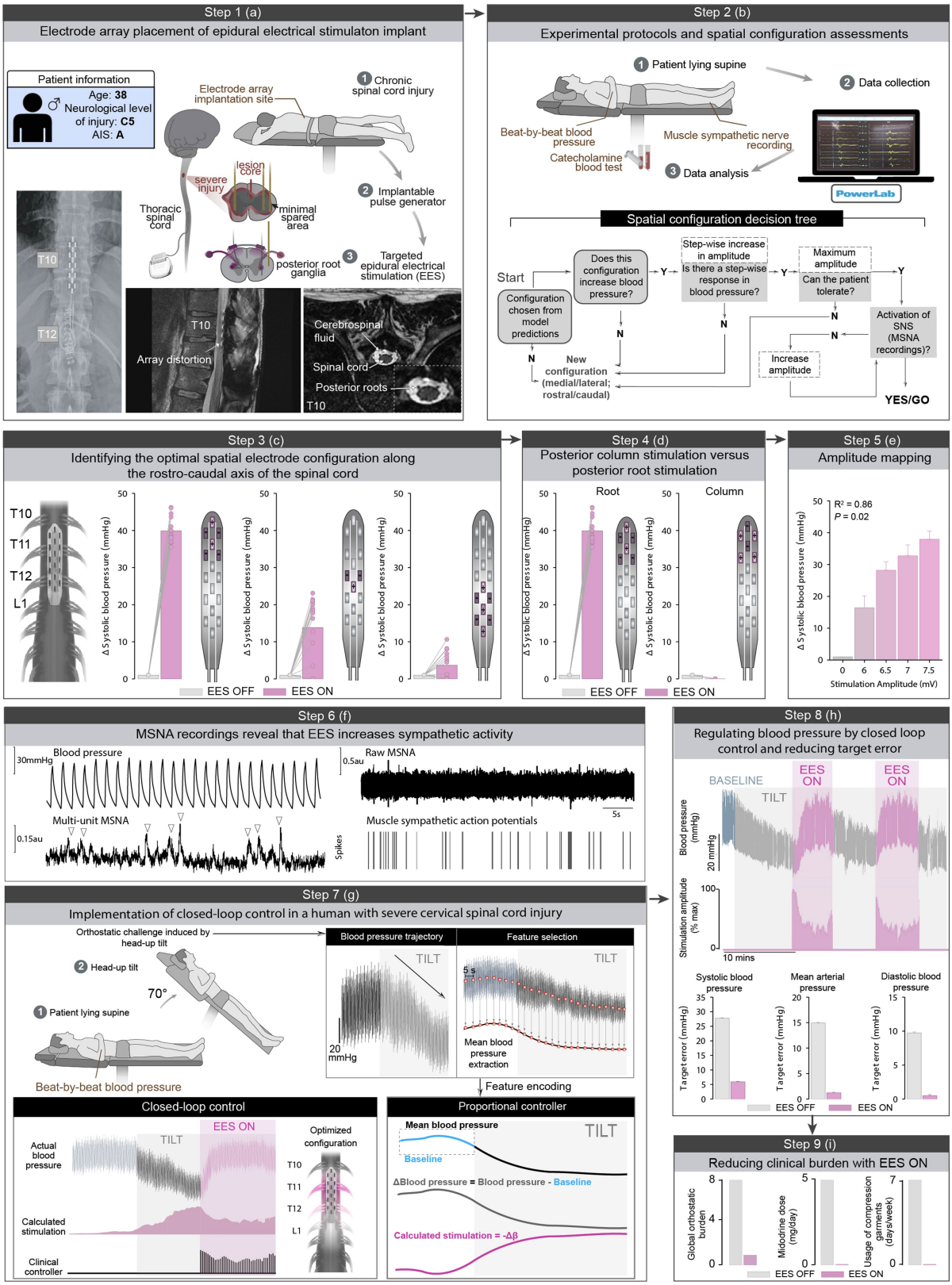

Extended Data Fig. 10 | See next page for caption.

Extended Data Fig. 10 | Targeted epidural electrical stimulation enables control of haemodynamics in a human with spinal cord injury. Step 1(a): A 5-6-5 Medtronic paddle array was implanted below the T10 and T11 vertebral bodies in a 38-year-old patient with clinically-complete cervical SCI, presenting with medically-refractory orthostatic hypotension. We confirmed the paddle array location with computerized tomography and magnetic resonance imaging. Step 2(b): We recorded haemodynamics, MSNA and catecholamine levels in the patient with and without stimulation. We used personalized computational modelling and a genetic algorithm to predict the ideal spatial configurations to activate the lower thoracic spinal segments. We then used the illustrated decision-making process to determine whether to move forward with the use of a given configuration. Step 3(c): We identified an optimal configuration, which recruited the lower thoracic spinal segments, increased blood pressure, normalized plasma noradrenaline levels, and increased muscle sympathetic nerve activity. We tested other configurations that are not optimally targeted to these roots and found the blood pressure responses were not robust. Step 4(d): Activation of the posterior columns using medial electrodes did not lead to a pressor response. Step 5(e): Using the optimal configuration, we found a stepwise increase in blood pressure as we increased the amplitude of stimulation ($R^2 = 0.86$; $P = 0.02$; linear regression). Data are mean ± s.e.m. Step 6(f): Blood pressure and MSNA recordings during EES. The top left panel shows the blood pressure recording and the bottom left panel shows the rectified and integrated (mean voltage) neurogram demonstrating multi-unit MSNA. Triangles identify the accepted multi-unit MSNA bursts (broad base width with a peak surpassing three times the noise width). The mean voltage neurogram is derived from the raw MSNA neurogram in the top right panel, which is the amplified and bandpass filtered neurogram. The bottom right tracing shows the MSNA action potential spike events over time that were derived from the raw MSNA neurogram above. Step 7(g): To test whether the concept of the neuroprosthetic baroreflex could be implemented in humans, we verticalized the patient to induce an orthostatic challenge while recording blood pressure. We performed feature extraction to obtain a rolling mean blood pressure, from which we calculated a continuous error (Δblood pressure). We then adjusted the weighted proportion to generate a calculated stimulation output, which was implemented using a clinician controller to modulate blood pressure in a closed loop. Step 8(h): When our closed-loop system was activated, blood pressure was tightly regulated evidenced by stabilized blood pressure and mitigated target error. Step 9(i): This patient now uses the stimulation daily and has been able to cease other treatments for orthostatic hypotension. Furthermore, the daily use of this therapy has reduced self-reported burden of orthostatic hypotension for this patient, as assessed using clinical questionnaires. AIS, American Spinal Injury Association Impairment Scale.

nature research

Corresponding author(s): Gregoire Courtine, Aaron A. Phillips

Last updated by author(s): Nov 7, 2020

Reporting Summary

Nature Research wishes to improve the reproducibility of the work that we publish. This form provides structure for consistency and transparency in reporting. For further information on Nature Research policies, see our Editorial Policies and the Editorial Policy Checklist.

Statistics

For all statistical analyses, confirm that the following items are present in the figure legend, table legend, main text, or Methods section.

n/a	Confirmed	
☐	☒	The exact sample size (*n*) for each experimental group/condition, given as a discrete number and unit of measurement
☐	☒	A statement on whether measurements were taken from distinct samples or whether the same sample was measured repeatedly
☐	☒	The statistical test(s) used AND whether they are one- or two-sided *Only common tests should be described solely by name; describe more complex techniques in the Methods section.*
☐	☒	A description of all covariates tested
☐	☒	A description of any assumptions or corrections, such as tests of normality and adjustment for multiple comparisons
☐	☒	A full description of the statistical parameters including central tendency (e.g. means) or other basic estimates (e.g. regression coefficient) AND variation (e.g. standard deviation) or associated estimates of uncertainty (e.g. confidence intervals)
☐	☒	For null hypothesis testing, the test statistic (e.g. *F*, *t*, *r*) with confidence intervals, effect sizes, degrees of freedom and *P* value noted *Give P values as exact values whenever suitable.*
☒	☐	For Bayesian analysis, information on the choice of priors and Markov chain Monte Carlo settings
☒	☐	For hierarchical and complex designs, identification of the appropriate level for tests and full reporting of outcomes
☒	☐	Estimates of effect sizes (e.g. Cohen's *d*, Pearson's *r*), indicating how they were calculated

Our web collection on statistics for biologists contains articles on many of the points above.

Software and code

Policy information about availability of computer code

Data collection	Data were collected using Labchart v8 (ADInstruments), Labview (2018 version 18.0), Zen2 Black (Zeiss), Imaris (9.1.2, 64Bit, Bitplane).
Data analysis	All softwares and software versions used to analyze data are described in the Method section at the relevant paragraph: Imaris, ImageJ, Labchart, MATLAB and R. A description is added to the method section when R or MATLAB custom-codes are used. Illustrations were generated using Autodesk 2020.2, Maya 2020.2, Adobe Illustrator CC 2015. R (version 3.6.0) was used for statistical evaluation, described in each method section using the following packages: Matrix (version 1.2-17), Polychrome (version 1.2.3), RColorBrewer (version 1.1-2), argparse (version 2.0.1), broom (version 0.5.2), colorspace (version 1.4-1), cowplot (version 1.0.0.9000), data.table (version 1.12.6), drlib (version 0.1.0), ggrepel (version 0.8.1), magrittr (version 1.5), openxlsx (version 4.1.0.1), patchwork (version 1.0.0), scales (version 1.0.0), stringr (version 1.4.0), tidyverse (version 1.2.1), WaveletComp (version 1.1), pracma (version 2.2.9), psd (version 2.1.0), signal (version 0.7-6), zoo (version 1.8-8), rmatio (version 0.14.0), flashClust (version 1.01-2) , FactoMineR (version 2.3), lme4 (version 1.1-23), imager (version 0.42.3), RNiftyReg (version 2.6.8), lmerTest (version 3.1-2), keras (version 2.3.0.0), tidymodels (version 0.1.1).

For manuscripts utilizing custom algorithms or software that are central to the research but not yet described in published literature, software must be made available to editors and reviewers. We strongly encourage code deposition in a community repository (e.g. GitHub). See the Nature Research guidelines for submitting code & software for further information.

Data

Policy information about availability of data

All manuscripts must include a data availability statement. This statement should provide the following information, where applicable:

- Accession codes, unique identifiers, or web links for publicly available datasets
- A list of figures that have associated raw data
- A description of any restrictions on data availability

Data that support the findings and software routines developed for the data analysis will be made available upon reasonable request to the corresponding author.

Field-specific reporting

Please select the one below that is the best fit for your research. If you are not sure, read the appropriate sections before making your selection.

☒ Life sciences ☐ Behavioural & social sciences ☐ Ecological, evolutionary & environmental sciences

For a reference copy of the document with all sections, see nature.com/documents/nr-reporting-summary-flat.pdf

Life sciences study design

All studies must disclose on these points even when the disclosure is negative.

Sample size	Sample sizes are estimated based on previous physiological studies using similar animal models to guarantee statistical relevance. Knowing the typical variance of blood pressure and histological quantitative analyses, we estimated that n=5 to 10 animals per group allows at least 80% statistical power when using the appropriate statistical test. No further sample size calculation was performed.
Data exclusions	For chronic hemodynamic and sympathetic nerve recordings two animals were excluded two to device malfunction.
Replication	All tested conditions were repeated across multiple trials and the results averaged to obtain a single-subject mean performance.
Randomization	Animals were randomly assigned to experimental groups when more than one condition was present. For within-animal or human comparisons every effort was made to randomize the order of conditions.
Blinding	In some cases blinding is not possible during data collection as the animals either have a SCI or do not. However, all statistical analysis was completed with the investigator blind to the experimental codings.

Reporting for specific materials, systems and methods

We require information from authors about some types of materials, experimental systems and methods used in many studies. Here, indicate whether each material, system or method listed is relevant to your study. If you are not sure if a list item applies to your research, read the appropriate section before selecting a response.

Materials & experimental systems

n/a	Involved in the study
☐	☒ Antibodies
☒	☐ Eukaryotic cell lines
☒	☐ Palaeontology and archaeology
☐	☒ Animals and other organisms
☐	☒ Human research participants
☒	☐ Clinical data
☒	☐ Dual use research of concern

Methods

n/a	Involved in the study
☒	☐ ChIP-seq
☒	☐ Flow cytometry
☒	☐ MRI-based neuroimaging

Antibodies

Antibodies used	The following primary antibodies were used: guinea pig anti-neuronal nuclei (NeuN, 1:300, Millipore, ABN90P), rabbit anti-cFos (cFos, 1:500, Calbiochem, PC38), mouse anti-tyrosine hydroxylase (TH, 1:2000, Millipore, MAB318), mouse anti-glial fibrillary acidic protein (GFAP, 1:1000, Sigma-aldricht, G3893), mouse anti-vesicular glutamate transporter 1 (VGLUT1, 1:1000, Millipore, MAB5502), rabbit anti-choline acetyltransferase (ChAT, 1:50, Millipore, AB144P) and rabbit anti-alpha 1 Adrenergic Receptor (ADRA1, 1:500, Abcam, AB3462. Secondary antibodies included: Alexa Fluor 647 Donkey Anti Mouse (1:200; Life Technologies, A31571), Alexa Fluor 488 Donkey Anti Rabbit (1:200, Life Technologies, A21206), Alexa Fluor 488 Goat anti Rabbit (1:200, Life Technologies, A11008), Alexa Fluor 555 Goat anti Rabbit (1:200, Life Technologies, A21428), Alexa Fluor 555 Goat anti Guinea Pig (1:200, Life Technologies, A21435) and also DAPI (1:1000, Life technologies). Following the secondary staining, three additional washes with PBS were performed and a Nissl stain was applied (1:100, Millipore).

Validation	The concentration of each antibody was tested before use and confirmed based on the morphology of positive signal.

Animals and other organisms

Policy information about studies involving animals; ARRIVE guidelines recommended for reporting animal research

Laboratory animals	Experiments were conducted on adult female Lewis rats (180–220 g body weight, 14–30 weeks of age) and adult male or female TH-Cre rats (180–400 g body weight, 14–30 weeks of age). Three healthy male Rhesus monkeys (Macaca mulatta) aged 5 years old, and weighing 5.4, 5.4 and 5.8 kg were used.
Wild animals	NA
Field-collected samples	NA
Ethics oversight	Procedures and surgeries were approved by the Veterinary Office of the Canton of Geneva (Switzerland; GE/87/17 and GE/212/17) and the University of Calgary (AC17-0185). Non-human primate experiments were approved by the Institutional Animal Care and Use Committee of China Academy of Medical Sciences in Beijing (LQ19003) and performed in accordance with the European Union directive of 22 September 2010 (2010/63/EU) on the protection of animals used for scientific purposes in an AAALAC-accredited facility (Chinese Academy of Science, Beijing, China), as we have previously described.

Note that full information on the approval of the study protocol must also be provided in the manuscript.

Human research participants

Policy information about studies involving human research participants

Population characteristics	The patient was a 38-year-old male who experienced a traumatic SCI at the C5 spinal segment treated with cervical fixation one year before enrollment in the study. The neurological status was evaluated according to the American Spinal Injury Association Impairment Scale (AIS) 24, and was classified as motor and sensory complete (AIS-A; Extended Data Fig. 10a).
Recruitment	The participant is highly educated and was in contact with many clinicians in clinics located at Foothills Hospital in Calgary. The participant voluntarily accepted to be involved in the proposed observational case study.
Ethics oversight	Clinical testing was approved by the University of Calgary Research Ethics Board (REB18-1592, REB19-0349).

Note that full information on the approval of the study protocol must also be provided in the manuscript.